JGR Solid Earth

RESEARCH ARTICLE
10.1029/2019JB017865

Contained Laboratory Earthquakes Ranging From Slow to Fast

Bill S. Wu[1] and **Gregory C. McLaskey**[1]

[1]School of Civil and Environmental Engineering, Cornell University, Ithaca, NY, USA

Key Points:

- We generate contained earthquake-like slip events on a 3 m dry, homogeneous granite fault that do not rupture through the sample ends
- We create a spectrum of slow to fast events, ranging from **M** −3.2 events with 50 kPa stress drop to **M** −2.5 quakes with 0.4 MPa stress drop
- Slow events produce tremor-like seismic radiation and have an ω^{-1} spectral shape that matches slow earthquakes in nature

Correspondence to:
G. C. McLaskey,
gcm8@cornell.edu

Citation:
Wu, B. S., & McLaskey, G. C. (2019). Contained laboratory earthquakes ranging from slow to fast. *Journal of Geophysical Research: Solid Earth*, *124*. https://doi.org/10.1029/2019JB017865

Received 16 APR 2019
Accepted 27 AUG 2019
Accepted article online 1 SEP 2019

Abstract Loading a 3-m granite slab containing a saw-cut simulated fault, we generated slip events that spontaneously nucleate, propagate, and arrest before reaching the ends of the sample. This work shows that slow (0.07 mm/s slip speeds) and fast (100 mm/s) contained slip events can occur on the same fault patch. We also present the systematic changes in radiated seismic waves both in time and frequency domain. The slow earthquakes are 100 ms in duration and radiate tremor-like signals superposed onto a low-frequency component of their ground motion. They are often preceded by slow slip (creep) and their seismic radiation has an ω^{-1} spectral shape, similar to slow earthquakes observed in nature. The fastest events have slip velocity, stress drop, and apparent stress (0.2 m/s, 0.4 MPa, and 1.2 kPa, respectively) similar to those of typical **M** −2.5 earthquakes, with a single distinct corner frequency and ω^{-2} spectral falloff at high frequencies, well fit by the Brune earthquake source model. The gap between slow and fast is filled with intermediate events with source spectra depleted near the corner frequency. This work shows that a fault patch of length p with conditions favorable to rupture can radiate in vastly different ways, based on small changes in $\frac{p}{h^*}$, where h^* is a critical nucleation length scale. Such a mechanism can help explain atypical scaling observed for low-frequency earthquakes that compose tectonic tremor.

Plain Language Summary Some faults slip slowly and silently, while others are locked and then slip spontaneously in an abrupt fashion. There is debate on whether slow and fast slip are distinct processes or lie on a continuum of fault slip modes in nature. Recent laboratory observations show that a single fault can slip in both modes and at some intermediate velocities, creating a spectrum of slow to fast earthquakes. We have conducted laboratory earthquake experiments where we force a fault cut in a 3-m-long granite rock to slip under pressure. The experiments show that by giving a rupture more distance to accelerate before it runs in to unfavorable fault conditions and dies, it can emit high-frequency energy more efficiently and exhibit resemblance to natural regular earthquakes. On the other hand, if a rupture barely accelerates before stopping, it will emit weak tremors. This proposed mechanism and the seismic consequences highlighted in this study may explain the puzzling behavior of deep tectonic tremor sometimes radiated from slow earthquakes.

1. Introduction

Since Brace and Byerlee (1966) first suggested stick-slip frictional instability as a mechanism for crustal earthquakes, laboratory experiments have explored topics ranging from friction properties (e.g., Dieterich & Kilgore, 1994), rupture dynamics (e.g., Johnson et al., 1973; Johnson & Scholz, 1976), and earthquake nucleation (e.g., Ohnaka & Kuwahara, 1990; Okubo & Dieterich, 1984). In laboratory experiments, fault stability is controlled by the loading system stiffness k and sample length l in relation to a critical stiffness k_c (Ruina, 1983) and a critical nucleation length h^* (Dieterich, 1992). When $k > k_c$, the laboratory sample will slide stably. When $k < k_c$ two types of stick-slip can occur: When $\frac{l}{h^*} \ll 1$, the sample slides like a rigid block and accelerates uniformly (Marone, 1998). When $\frac{l}{h^*} \gg 1$, the transition from slow to rapid slip is commonly modeled as an expanding shear rupture (e.g., Andrews, 1976; Ben-David et al., 2010; Rosakis et al., 2006). In this model, localized slow aseismic slip within an h^*-sized region on the fault occurs before rapid, seismic slip commences, in a process known as earthquake nucleation (Kato et al., 1992; McLaskey & Kilgore, 2013; Nielsen et al., 2010; Ohnaka & Kuwahara, 1990; Okubo & Dieterich, 1984; Selvadurai & Glaser, 2017).

A family of slow earthquakes have been observed in the past 20 years with the deployment of continuous GPS recording systems and high-sensitivity borehole seismometers and strain meters. Independent

discoveries of periodic deep tremor and slow slip events (SSE) in Japan (Hirose et al., 1999; Obara, 2002) and Cascadia (Dragert et al., 2001) led Rogers and Dragert (2003) to recognize their connection and name the phenomenon episodic tremor and slip (ETS). Other members of the slow earthquake family include low-frequency earthquakes (LFEs), very low frequency (VLF) earthquakes, and silent earthquakes. Shelly et al. (2007) showed that tectonic tremor is a swarm of LFEs. All of these events are associated with slip on the plate interface, but they have low stress drop relative to standard earthquakes and originate either downdip or updip of the seismogenic zone, in regions where a transition between unstable and stable frictional properties is expected to occur (Beroza & Ide, 2011; Liu & Rice, 2005; Obara & Kato, 2016; Scholz, 1988; Schwartz & Rokosky, 2007).

Recent laboratory experiments have explored the transition between stable and unstable behavior to probe the mechanics of slow earthquake phenomena (Kaproth & Marone, 2013; Leeman et al., 2016; Scuderi et al., 2016). Slow earthquakes in the lab occur when the machine loading stiffness approaches the critical stiffness (Leeman et al., 2016) or the sample length approaches the critical nucleation length (McLaskey & Yamashita, 2017). In the latter, a slow-slip event was produced when a nucleating slip event did not accelerate to fully seismic speeds before the rupture reached the ends of the sample and could not propagate any further.

We have designed a 3-m biaxial direct shear rock friction machine with $l > h^*$. In addition to traditional "complete rupture" stick-slip events, it produces contained rupture events that nucleate within the sample and arrest before reaching the sample ends (Ke et al., 2018). To our knowledge, no other rock friction apparatus can create contained rupture events, except via pore fluid injection (Lockner et al., 1982). The contained events are generated through a specified loading procedure that creates a heterogeneous stress state along the 3-m fault. The fault must contain a patch of length p with stress conditions that are favorable for rupture propagation, and outside of patch p, rupture rapidly terminates due to unfavorable stress conditions. A contained dynamic slip event will only occur if $h^* < p < l$.

In experimental runs lasting tens of minutes, we can generate sequences of slip events that grow from slow to fast. Initially $p \leq h^*$, thereby events terminate before accelerating to fully seismic speeds. With continued loading, the ratio $\frac{p}{h^*}$ increases and successive events become larger and faster. A spectrum of slow to fast contained and partially contained events are produced before the entire fault ruptures dynamically in standard stick-slip fashion. The fastest contained events generated have maximum slip velocity, stress drop, and apparent stress (0.2 m/s, 0.4 MPa, and 1.2 kPa, respectively) similar to ordinary $\mathbf{M}$ −2.5 earthquakes. The slower slip events have low static stress drops (20–100 kPa), and peak slip velocities that range from 0.1–10 mm/s.

The containment of the events on a simulated fault provides a unique opportunity to study the source parameters—moment, stress drop, and radiated energy—of laboratory earthquakes that initiate and terminate primarily due to properties of the rock, with little influence from the machine loading stiffness k. Both the sample and loading apparatus affect k, which is roughly defined as the increase in sample average shear stress that occurs from a unit advancement of the loading piston (see, e.g., McLaskey & Yamashita, 2017). The contained events do rupture through the top and bottom free surfaces of the slab, but this has more minor effects on their characteristics. Using an array of local fault slip measurements, we measured the static stress drop of the contained events. Piezoelectric sensors were used to quantify the source spectra of the events. We find that near $\frac{p}{h^*} \approx 1$, moderate variations in p or h* can strongly affect stress drop and maximum slip velocity and produce orders of magnitude variation in radiated energy. The laboratory-generated slow slip events are depleted in energy near the corner frequency and the recorded laboratory seismograms contain a tremor-like high-frequency component superposed upon a low-frequency component, similar to natural VLF events (e.g., Ghosh et al., 2015).

In this work, we first describe the laboratory experiments, typical loading sequences, and how we classify events based on the spatial distribution of slip and maximum slip rate. Section 3 describes how the moment and stress drop of the contained events are determined both geodetically, from local fault slip measurements, and seismically, from the spectra of their radiated waves. Section 4 presents examples of slow to fast events and illustrates the systematic variation in their initiation processes, ground motions, and spectral shapes. Finally, we present a model to explain the mechanism behind their variation and compare the laboratory events to slow and fast earthquakes observed in nature.

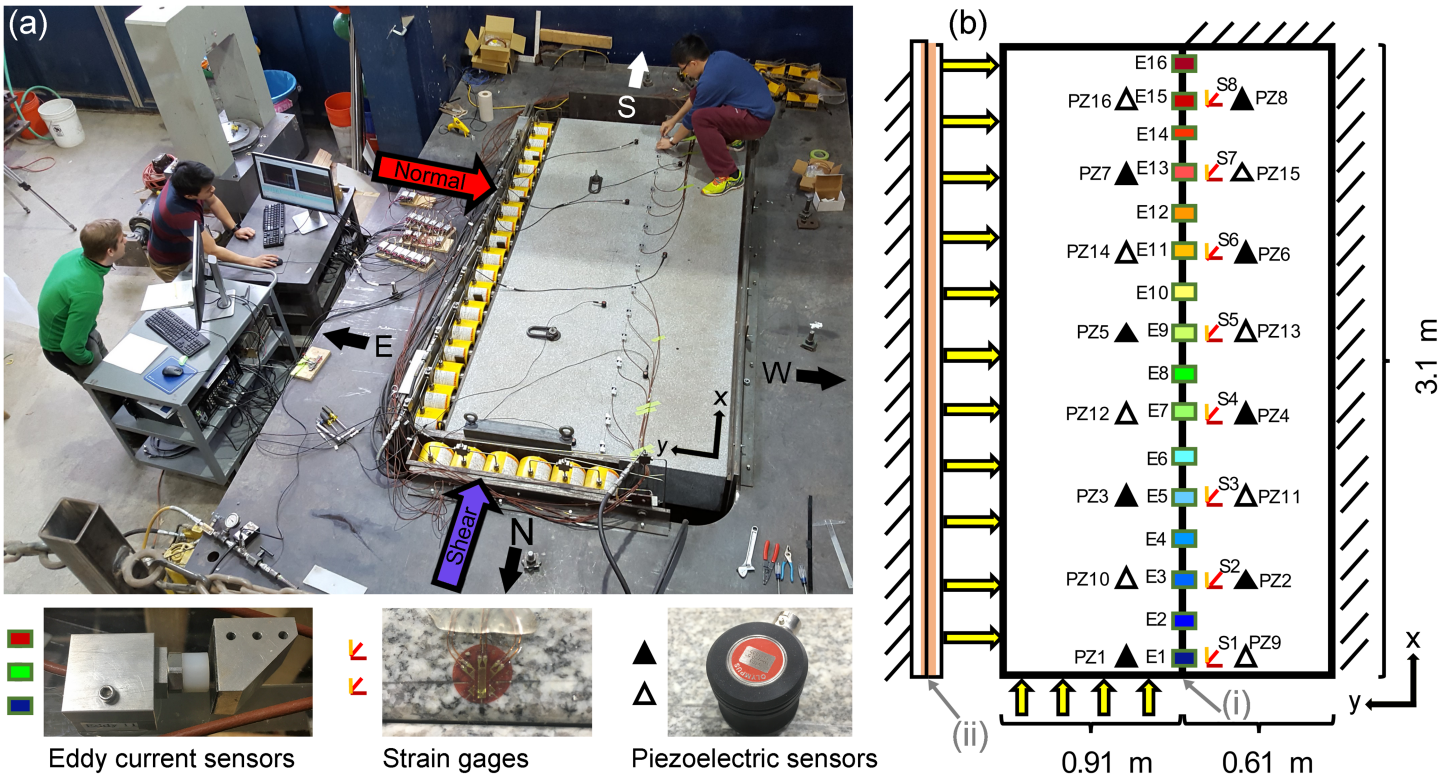

Figure 1. (a) Annotated photograph and (b) schematic diagram of the sample and apparatus. The two granite samples are 3.1 m long and are placed into a steel loading frame using an overhead crane. Forces are applied to the samples with 54 hydraulic cylinders (36 for normal force and 18 for shear force, as labeled). Slip sensors (E1–E16), strain gages (S1–S8), and piezoelectric sensors (PZ1–PZ16) are coupled to the top and bottom surfaces. The locations of slip sensors are denoted by rectangles colored from blue (North end) to red (South end). Open and filled triangles describe piezoelectric sensors on the top and bottom of the sample, respectively. Slip occurs on the (i) rock-rock interface and (ii) Teflon-steel low-friction interface.

2. Mechanics of the Experiment

2.1. Overview

A photograph and schematic diagram of our biaxial direct shear apparatus, hereafter referred to as the "Cornell 3 m apparatus," is shown in Figure 1. Two 3.1-m-long rectangular Barre gray granite blocks are squeezed together and sheared past one another. Slip occurs on (i) a dry, rock-rock interface between the moving and stationary blocks and (ii) a Teflon-steel low-friction interface (LFI). The dimensions of the moving block are 3,100 mm × 910 mm × 310 mm in the x, y, and z directions, and dimensions of the stationary block are 3,150 mm × 610 mm × 310 mm. The simulated fault is 3,100 mm × 310 mm with area A= 0.961 m^2.

We conducted sets of ~3-hr-long experiments, once every 1–6 weeks over about 24 months. After the fault had slipped approximately 40 mm over many experiments, we unloaded the sample completely, retracted the cylinders, and reset the moving block and eastside hydraulic cylinders using an overhead crane. During this procedure, the two rocks were separated and the fault surface roughness was measured with a profilometer at seven locations in October 2018 and had a mean roughness of ~7 μm. A small amount of fine rock flour (fault gouge) was distributed throughout the nominal area of contact. Upon close inspection, striations tens of millimeters in length in the x direction were dispersed across the fault surface. Large concentrations of striations and an overall roughening of the fault surface was observed within 50 mm of the fault ends all across its width (z direction). Fault gouge was not removed between experiments or when we separated the rocks.

2.2. Instrumentation

Eddy current sensors (E1–E16, sampled at 50 kHz then averaged to 5 kHz) measured local slip $\delta(x,t)$ on the simulated fault surface at 16 equally spaced locations (Figure 1b). Local strain was measured by eight strain

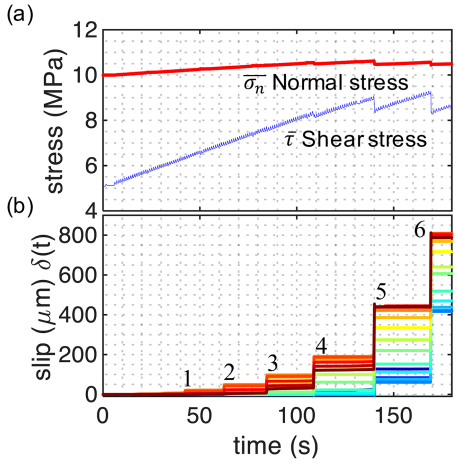

Figure 2. Loading procedure and slip time history in an experiment. (a) Sample-averaged normal and shear stress derived from hydraulic pressure. (b) Slip time history recorded from the eddy current sensors (E1–E16). The lines are color coded based on the location of eddy current sensor as shown in Figure 1b. Slip events 1–6 are labeled. Event 5 is the first event to rupture the entire 3.1-m fault.

gage rosettes (S1–S8, sampled at 100 Hz) collocated with odd-numbered slip sensors. Each rosette consisted of three collocated 5-mm-long strain gages oriented at 45°, 90°, and 135° from the fault. Local stresses σ_{xx}, σ_{yy}, and σ_{xy} were derived from these strain components and elastic properties of Barre gray granite, shear modulus G=30 GPa and Poisson ratio $\nu = 0.23$. Sample-average normal and shear stresses ($\overline{\sigma_n}$ and $\overline{\tau}$, respectively), labeled by an overbar, were derived from hydraulic pressure measurements, described in section 2.3.

An array of 16 Panametrics V103 ultrasonic piezoelectric sensors, sampled at 1 MHz, were coupled to the granite blocks using superglue on both the top (PZ1–PZ8) and bottom surfaces (PZ9–PZ16) to measure ground motion in the z direction. Output from these sensors is approximately proportional to vertical ground displacement in the 60- to 700-kHz band and acceleration in the 1- to 10-kHz band (Wu & McLaskey, 2018).

2.3. Loading and Stress Profiles

Figure 2 describes the loading procedure and slip time history $\delta(t)$ of a typical experimental run using experiment FS01_27_10MPaP as an example. Force was applied to the granite samples by advancing hydraulic cylinders using an Enerpac P-462 hydraulic hand pump.

In a typical loading sequence, $\overline{\sigma_n}$ was increased to a specified level between 1 and 12 MPa and then held approximately constant by closing a valve such that the volume of hydraulic fluid remained constant in the 36 Eastside cylinders. Normal stress was still weakly coupled to shear stress through the Poisson effect. Shear stress $\overline{\tau}$ was then increased at a relatively steady rate $\dot{\tau} = 0.03$ MPa/s by increasing the hydraulic pressure in the 18 northside cylinders, somewhat analogous to slow tectonic loading (Figure 2a). This produced sequences of events with a roughly constant recurrence interval.

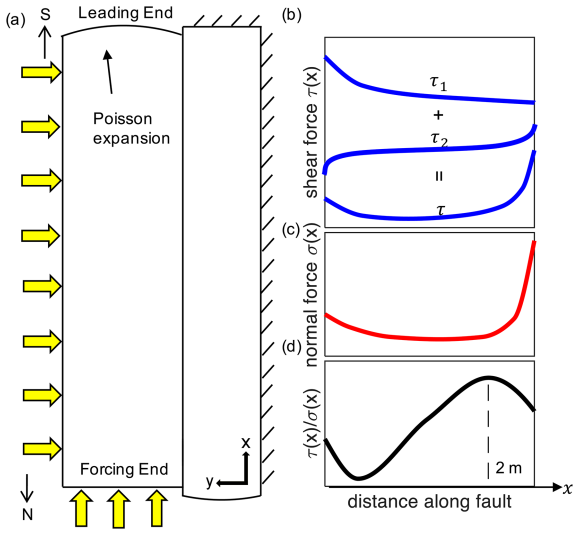

Figure 3. Normal and shear stress heterogeneity created by the Poisson expansion loading scheme. $\overline{\sigma_n}$ is increased to a prescribed level, and then $\overline{\tau}$ is slowly increased to generate a sequence of slip events. (a) When loaded in the y direction, the moving block expands in the x and z directions, while the stationary block is constrained on the south and west edges; (b) a nonuniform shear stress profile $\tau(x)$ is created from the local application of shear stress τ_1 and the frustrated Poisson expansion τ_2; (c) nonuniform normal stress profile that results from sample edge effects, compliance of the load frame, and shear-force-induced torque; (d) as a result, the $\tau(x)/\sigma(x)$ ratio has a maximum at around 2 m and this is where slip events are observed to nucleate.

Large increases in applied $\overline{\sigma_n}$ (e.g., 1 to 4 MPa or 4 to 10 MPa) created heterogeneous shear stress profiles across the fault. Figure 3 illustrates the frustrated Poisson expansion that occurs on the moving block during loading and a schematic of the resulting stress profiles. Nonuniformity of $\tau(x)$ has two main sources. First, the localized application of shear force creates an increase of shear force at the north end (Figure 3b, τ_1). Second, when the normal load was increased from 4 to 10 MPa (while $t < 0$, not shown in Figure 2a), the applied force in the y direction caused the moving block to expand in the x and z directions, that is, "Poisson expansion," while the stationary block is thinner in the y direction and is constrained from expanding on its S and W sides. As a result, local shear stress on the fault increased at the south end and decreased at the north end (Figure 3b, τ_2), creating heterogeneous shear stress profile $\tau = \tau_1 + \tau_2$. The bowl-shaped $\sigma(x)$, which is common to these type of experiments (Ke et al., 2018; Yamashita et al., 2018), results from (1) the torque exerted on the moving block by the application of shear stress, (2) compliance of the steel loading frame, and (3) edge effects. As a result, the peak τ/σ ratio consistently occurs ~2 m from the north end of the fault (Figure 3d). The $\tau(x)$ and $\sigma(x)$ measured by the strain gages and simulated through finite element models support the general trends described in Figure 3 (Ke et al., 2018).

Hereafter, we refer to the series of events generated after a large increase in $\overline{\sigma_n}$ as a Poisson expansion sequence. For catalog purposes the sequence in Figure 2 is called "FS01_27_10MPaP", which denotes the Poisson expansion sequence at $\overline{\sigma_n} = 10$ MPa in the 27th overall day of experiments on the first set of blocks used on the Cornell 3 m apparatus.

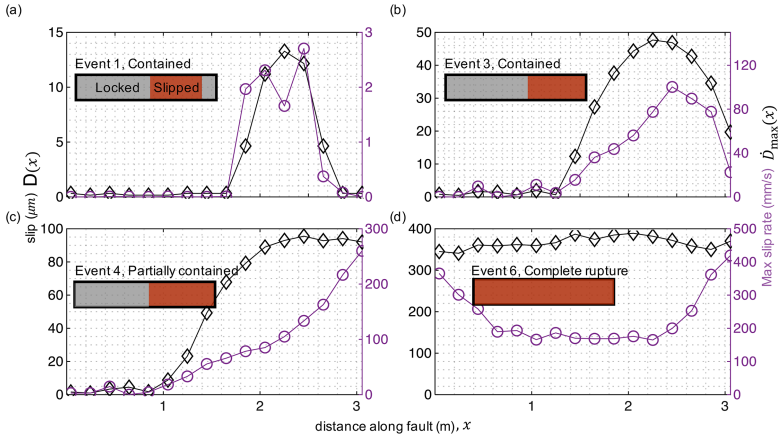

Figure 4. Three kinds of laboratory earthquakes, categorized by slip distribution $D(x)$ (diamonds) and peak slip rate distribution $\dot{D}_{max}(x)$ (circles). (a) Contained event, (b) contained event, (c) partially contained event, and (d) complete rupture.

Fault slip time history $\delta(t)$ is shown in Figure 2b. Events 1–4 were the result of slip on some but not all of the fault. They occurred before $\overline{\tau}$ reached the sample average critical stress $\overline{\tau_{crit}}$ and showed essentially no sample average stress change $\Delta\overline{\tau}$, as measured on the hydraulic pressure sensor. ($\overline{\tau_{crit}}$ is the maximum $\overline{\tau}$ the sample can withstand, as shown in Figure 2a.) For events 1–4, $\tau(x)/\sigma(x)$ exceeded a critical value near $x = 2$ m, but $\tau(x)/\sigma(x)$ was not uniform enough for the rupture to propagate through the entire sample. Events 5 and 6 ruptured the entire 3-m fault. These events occurred when $\frac{\overline{\tau_{crit}}}{\overline{\sigma_n}} = \overline{\mu_{crit}} \cong 0.8$. This value of $\overline{\mu_{crit}}$ is higher than the typical static friction coefficient μ_s for granite due to the contribution from the Teflon-steel LFI ($\overline{\mu_{crit}} = \mu_s + \overline{\mu_{LFI}}$). We estimate that $\overline{\mu_{LFI}} = 0.1$–$0.13$ based on previous work using a similar LFI (McLaskey & Yamashita, 2017).

2.4. Three Types of Events: Contained, Partially Contained, Complete Rupture

Using slip measurements $\delta(x,t)$ from the 16 eddy current sensors, we defined parameters for each slip event. The spatial distribution of slip $D(x)$ was defined as the slip that occurred in a 1-s time window surrounding the event. The max slip rate distribution, $\dot{D}_{max}(x)$, was estimated numerically from the slip sensor recording $\delta(t)$ at location x: $\dot{D}_{max}(x) = \max\left(\dot{D}(x,t)\right)$ where $\dot{D}(x,t) = (\delta(x,t) - \delta(x,t-\Delta t))/\Delta t$, and Δt is the sampling period. For slow events, low-pass filters were applied during the calculation of $\dot{D}(x,t)$ to reduce high-frequency noise that was accentuated as a result of the numerical differentiation. For each event, we also defined the event max slip rate $\dot{D}_{max} = \max\left(\dot{D}_{max}(x)\right)$ excluding outliers and edge effects.

Across all experiments, we categorized the observed events by the shape of their slip distribution $D(x)$ and peak slip rate distribution $\dot{D}_{max}(x)$ into three types: (1) contained, (2) partially contained, and (3) complete rupture (Figure 4). For contained events, both $D(x)$ and $\dot{D}_{max}(x)$ have a maximum at the center of the ruptured region and taper off gradually toward the edges (Figure 4a). We classify an event as contained even if it has a finite amount of slip at the south end of the sample (Figure 4b), as long as $\dot{D}_{max}(x)$ at the south end is less than 50% of the event max slip rate, $\max(\dot{D}_{max}(x))$. This allows us to classify as fully contained those events where rapid dynamic slip was halted but slow afterslip continued near the sample edge. For partially contained events, $D(x)$ and $\dot{D}_{max}(x)$ taper off to zero on one side of the ruptured region, but either $D(x)$ or $\dot{D}_{max}(x)$ does not decrease on the other side (Figure 4c). The main identifier for a partially contained event is $\dot{D}_{max}(x)$ increases near the sample edge, likely due to an edge effect. In contrast, events classified as fully contained show a sharp decrease in $\dot{D}_{max}(x)$ near the sample edge (Figure 4b).

Complete rupture events (Figure 4d) propagate across the entire fault surface and are similar to stick-slip instabilities observed previously (Brace & Byerlee, 1966; Dieterich, 1981; Johnson & Scholz, 1976; Togo et al., 2015). $D(x)$ is approximately uniform across the fault, while the aforementioned edge effect causes

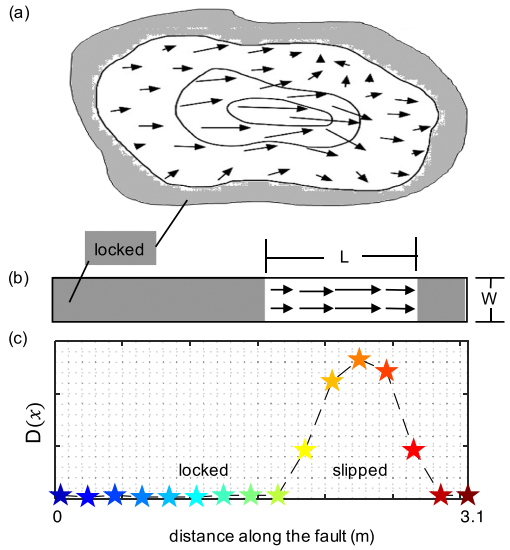

Figure 5. Schematic of fault slip on a natural fault and its simplification on our simulated fault. (a) Slip within the rupture zone (white background) on a natural fault is variable in space and time and surrounded by a nonslipping locked zone (gray), adapted from Stein and Wysession (2003). (b) Slip on our simulated fault surface is assumed to be uniform across its width W. L is the characteristic rupture length. (c) An example of the measured distribution of slip $D(x)$ is color coded with E1–E16 from Figure 1b.

an increase in $\dot{D}_{\max}(x)$ at the two sample ends (Figure 4d). This edge effect has also been observed on other large-scale rock experiments (McLaskey, Kilgore, et al. (2015), Figure 3).

Across all Poisson expansion sequences, we see a consistent progression of the three types of events. As $\overline{\tau}$ is steadily increased, a few contained and partially contained events will occur prior to the first complete rupture (when $\overline{\tau} = \overline{\tau_{\text{crit}}}$), after which $\overline{\tau}$ drops to a sample-averaged final stress level $\overline{\tau_f}$. Hereafter, complete rupture events occur at a roughly constant recurrence interval of $\frac{\overline{\tau_{\text{crit}}} - \overline{\tau_f}}{\dot{\tau}}$.

3. Methods

3.1. Geodetic Moment M_0^g

The distribution of slip during an earthquake on a natural fault and a schematic explanation of its simplifications are described in Figure 5. The rupture involves a complicated slip process that varies with space and time (Figure 5a). The scalar seismic moment M_0 is an integral of the process $M_0 = G\iint_S D(x,z)\mathrm{d}S$ and is often simplified $\mathrm{M}_0 = GA\overline{D}$ (Aki, 1966), where G is the shear modulus, A is the ruptured fault area, and $\overline{D}$ is the average slip over the rupture area. For natural earthquakes A is typically inferred from mapping the extent of aftershocks (Mogi, 1968), and $\overline{D}$ can be directly measured only if the rupture breaks the surface of the Earth. On our simulated fault surface, however, we measure the slip distribution $D(x)$ from slip measurements and assume that $D(x,z)$ is uniform throughout the fault width W (Figure 5b). We then define our estimate of the moment,

$$M_0^g = GW\int_0^{3\ \mathrm{m}} D(x)\mathrm{d}x, \tag{1}$$

where the superscript "g" denotes that seismic moment was computed geodetically.

The assumption of uniform $D(x)$ across W is supported by measurements of slip on the bottom surface of the granite slab, made for some experiments.

3.2. Source Spectrum From an Empirical Green's Function Approach

We estimated the radiated energy and the seismic moment of some slip events using the piezoelectric sensor array. The ground motion signal $s(t)$ recorded from a piezoelectric sensor is the combined effect of the source, wave propagation, and recording system. Sources occurring inside a body can be represented by a second-order moment tensor $m(t)$ (Aki & Richards, 1980). A Green's function $g(t)$ represents wave propagation effects such as geometric spreading, scattering, and attenuation. We combined the effects of the recording system, including the sensor response, coupling, digitizer, and cables, into an instrument response term $i(t)$ such that

$$s(t) = m(t)\otimes g(t)\otimes i(t), \tag{2}$$

where $\otimes$ represents convolution. In this work, we study the moment rate spectrum $\dot{M}(\omega)$, which is the first temporal derivative of the Fourier transform of $m(t)$ and is commonly referred to as the displacement source spectrum (e.g., Baltay et al., 2010).

The ideal displacement source spectrum of an earthquake is shown in Figure 6, alongside four spectra from lab-generated earthquakes. The ideal spectrum is flat with a constant low-frequency amplitude Ω_0 below the corner frequency f_0 and falls off with a high-frequency spectral decay of the form $\omega^{-\gamma}$ for $\omega > f_0$. The parameter f_0 is inversely proportional to the event duration. Ω_0 of the source spectrum $\dot{M}(\omega)$ is equal to M_0. The falloff rate is $\gamma = 2$ for most earthquake source models (e.g., Brune, 1970).

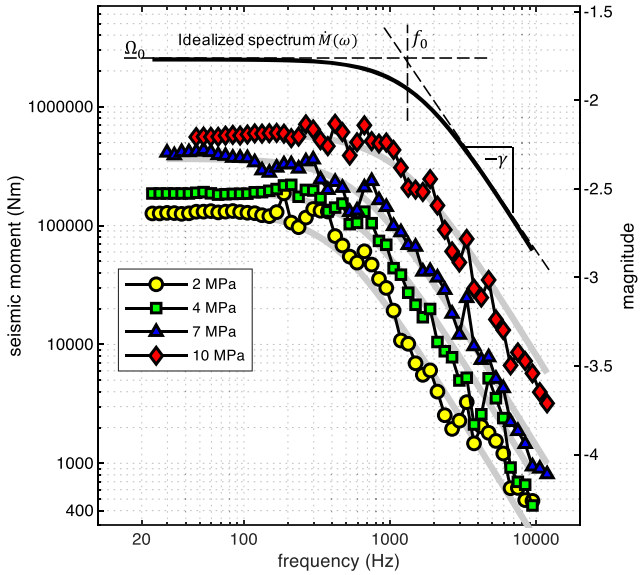

Figure 6. Idealized and estimated displacement source spectra $\dot{M}(\omega)$ of lab-generated earthquakes. Important features include the low-frequency amplitude Ω_0, corner frequency f_0, and falloff rate at high frequencies γ. Estimated source spectra were fitted to a Brune source model (gray lines). (Note that we observe an increase in f_0 with M_0, different from typical earthquake scaling relations. This is caused by the slow speed and low stress drop of the smaller events as described in section 5.1.)

We found $\dot{M}(\omega)$ of the slip events using a laboratory version of the empirical Green's function (EGF) approach (McLaskey, Lockner, et al., 2015). In this approach, $g(t)$ and $i(t)$ are common to both the EGF source and the seismic event to be analyzed, therefore the unknown source can be determined if the source of the EGF event is known. We used both ball impacts and one small abrupt contained event as EGF sources, and the method is described in Appendix A.

Once $\dot{M}(\omega)$ for an event was obtained (equation (A1)), the seismic moment M_0^s was found by averaging over the low frequencies of $\dot{M}(\omega)$ where the spectrum is relatively flat. There was good agreement between M_0^s and M_0^g for the contained events (see Table 1), and this provided a means of double-checking our seismic analysis. M_0^s was then used to constrain a Brune (1970) source model $\dot{M}(\omega) = M_0^s/\left(1 + (\omega/f_0)^2\right)$ to find the corner frequency f_0 by minimizing the sum of squared residuals between $\dot{M}(\omega)$ and the Brune model. Figure 6 shows the source spectra and Brune model fit for four contained and partially contained events. The source properties (f_0, M_0^g, M_0^s, etc.) are cataloged in Table 1.

3.3. Static Stress Drop for Contained Rupture Events

The stress drop of contained and partially contained events (Types 1 and 2) cannot be ascertained from sample average measurements (Figure 2a). Instead, for these events, we determined the static stress drop with methods analogous to those employed for the study of natural earthquakes. We begin with a conventional definition for static stress drop following Kanamori and Anderson (1975),

$$\Delta\sigma_{\text{static}} = CG\frac{\overline{D}}{L}, \tag{3}$$

where $\overline{D}$ is the average slip and is assumed to be half of the maximum slip max($D(x)$), L is the characteristic rupture length, C is a shape factor, and we assume $C = 2/\pi$ which is appropriate for long, strike-slip faults (Knopoff, 1958). Stress drop calculated using equation (3) was independently validated using strain gage measurements and a dislocation model in Appendix B.

4. Geodetic and Seismic Observation of Slow to Fast Earthquakes

4.1. Slip Measurements

Figures 7–9 present four example events that range from slow to fast. Events 29–32 are from a sequence at $\overline{\sigma_n} = 4$ MPa that produced slow and intermediate events. Event 42 is an example of one of the fastest contained events recorded. Generated at $\overline{\sigma_n} = 10$ MPa, Event 42 is the first event after an imposed hold where the loading rate $\dot{\tau}$ was set to zero for about 300 s and the fault rested in essentially stationary contact.

Figure 7 shows the recorded slip time history $\delta(t)$ for the two sequences and illustrates the different slip patterns that precede the slow and fast events. In general, experiments with slow, quasi-static creep, such as shown in Figure 7a tended to produce sequences of slow slip events that became progressively faster with successive events. Prior to event 29, slip rate increased nonlinearly for ~100 s from 0.1 to 0.5 μm/s. Sequences at higher $\overline{\sigma_n}$, and particularly after imposed holds, such as the sequence of Figure 7b, had minimal slow slip and produced faster events. Prior to Event 42, the fault was essentially locked with no observable preslip. Some slow slip preceded later events of this sequence.

4.2. Initiation and Arrest of Laboratory Earthquakes

Figure 8 shows the initiation of the same four selected events by plotting slip in 1.4-s time windows around each event. Each pink or purple contour shows a snapshot of the slip distribution along the fault, relative to the slip measured at the beginning of the time window. The contours are drawn every 5 ms and

Table 1
The Seismic and Mechanical Source Properties of 52 Events

Event #	FS01	Sequence	$\overline{\sigma_n}$ MPa	Time (s)	Type	$\dot{D}$max (mm/s)	D_{max}	L (m)	f_0 (Hz)	Mechanical M_0 (N m)	Seismic M_0 (N m)	Static stress drop (N/m^2)	Radiated energy (N m)
1	24	1MPaP	1	21	3	5.2	NA	3.1	NA	6.84E+05	7.24E+04	NA	NA
2	24	1MPaP	1	23	3	7.2	NA	3.1	NA	7.99E+05	9.40E+04	NA	NA
3	24	1MPaP	1	25	3	7.2	NA	3.1	NA	7.78E+05	9.08E+04	NA	NA
4	24	1MPaP	1	27	3	8.4	NA	3.1	NA	8.26E+05	8.71E+04	NA	NA
5	24	1MPaP	1	28	3	8.5	NA	3.1	NA	8.17E+05	8.20E+04	NA	NA
6	27	2MPaP	2	108	1	0.2	5.8	2	NA	7.40E+04	NA	2.82E+04	NA
7	27	2MPaP	2	123	2	8.9	14.9	2.2	NA	2.26E+05	NA	6.46E+04	NA
8	32	2MPaP	2	141	2	17.4	22.6	3.3	600	4.29E+05	1.29E+05	6.53E+04	1.21E−04
9	32	2MPaP2	2	77	1	0.1	5	2.3	NA	7.25E+04	NA	2.06E+04	NA
10	32	2MPaP2	2	81	2	9.6	15.4	2.9	420	2.88E+05	1.06E+05	5.06E+04	2.65E−05
11	15	4MPaP	4	37	1	16.3	13.4	1.5	NA	1.19E+05	NA	8.56E+04	NA
12	15	4MPaP	4	61	1	21.3	19.2	1.9	NA	2.09E+05	NA	9.92E+04	NA
13	15	4MPaP	4	96	2	30.7	46.9	2.9	NA	6.36E+05	NA	1.54E+05	NA
14	18	4MPaP	4	19	1	29	14.2	1.5	NA	1.19E+05	NA	9.07E+04	NA
15	18	4MPaP	4	32	1	16.3	14.9	1.7	NA	1.55E+05	NA	8.36E+04	NA
16	18	4MPaP	4	42	1	22.1	21.8	2	NA	2.70E+05	NA	1.04E+05	NA
17	18	4MPaP	4	56	2	39.6	44.6	3.1	NA	6.69E+05	NA	1.38E+05	NA
18	19	4MPaP	4	18	1	1.4	2.7	0.9	NA	1.50E+04	NA	3.06E+04	NA
19	19	4MPaP	4	28	1	14.6	8.6	1.2	NA	5.81E+04	NA	7.18E+04	NA
20	19	4MPaP	4	40	1	29.7	17	1.7	NA	1.59E+05	NA	9.53E+04	NA
21	19	4MPaP	4	52	2	49.2	50.9	2.6	NA	6.86E+05	NA	1.87E+05	NA
22	23	4MPaP	4	97	1	2.6	8.5	1.5	NA	6.83E+04	NA	5.40E+04	NA
23	23	4MPaP	4	121	1	25.7	17.1	1.7	NA	1.83E+05	NA	9.62E+04	NA
24	23	4MPaP	4	140	1	23.6	32.6	2.3	NA	4.62E+05	NA	1.36E+05	NA
25	26	4MPaP	4	67	1	23.2	20.8	2	620	2.33E+05	1.91E+05	9.94E+04	4.05E−04
26	26	4MPaP	4	117	3	74.6	NA	3.1	NA	4.15E+06	4.84E+05	NA	NA
27	26	4MPaP	4	186	3	99.9	NA	3.1	NA	5.48E+06	6.38E+05	NA	NA
28	26	4MPaP	4	194	3	54.1	NA	3.1	NA	3.25E+06	4.01E+05	NA	NA
29	35	4MPaP	4	223	1	0.54	9.64	2	NA	1.11E+05	1.82E+04	4.61E+04	9.61E−09
30	35	4MPaP	4	240	1	1.71	13.2	2.1	140	1.67E+05	1.01E+05	6.08E+04	6.74E−07
31	35	4MPaP	4	256	1	1.75	14.2	2.3	140	1.99E+05	9.60E+04	5.99E+04	6.38E−07
32	35	4MPaP	4	274	2	8.73	31.8	4	NA	4.38E+05	2.31E+05	7.59E+04	4.61E−05
33	19	7MPaP	7	20	1	5.4	7.5	0.9	NA	2.53E+04	NA	8.45E+04	NA
34	19	7MPaP	7	34	1	41.9	22.7	1.3	NA	1.64E+05	NA	1.67E+05	NA
35	26	7MPaP2	7	5	1	21.1	19.2	1.7	500	1.72E+05	1.62E+05	1.08E+05	7.91E−05
36	26	7MPaP2	8	24	2	59.6	45.9	2.1	620	5.73E+05	3.65E+05	2.09E+05	9.64E−04
37	26	7MPaP2	8	41	2	60.4	77.8	3.1	NA	1.14E+06	NA	2.40E+05	NA
38	26	7MPaP2	7	82	3	114.9	NA	3.1	NA	6.34E+06	1.08E+06	NA	NA
39	26	7MPaP2	7	108	3	191.2	NA	3.1	NA	8.45E+06	1.00E+06	NA	NA
40	24	10MPaP1	10	29	1	9.9	15.2	0.9	560	8.19E+04	6.22E+04	1.61E+05	4.62E−06
41	24	10MPaP1	10	59	1	22.9	20.5	1.3	1040	1.56E+05	1.30E+05	1.51E+05	8.30E−05
42	24	10MPaP2	10	37	1	92.3	57.6	1.8	1180	6.35E+05	5.87E+05	3.06E+05	3.13E−03
43	27	10MPaP	10	42	1	2.5	13.3	1.1	NA	8.76E+04	NA	1.15E+05	NA
44	27	10MPaP	10	62	1	36.3	27.4	1.4	NA	2.39E+05	NA	1.87E+05	NA
45	27	10MPaP	10	84	1	59.1	47.7	2	NA	5.61E+05	NA	2.28E+05	NA
46	27	10MPaP	11	109	2	71.3	95.5	2.9	NA	1.36E+06	NA	3.15E+05	NA
47	35	10MPaP	10	136	1	3.19	24.7	1.9	120	2.36E+05	1.22E+05	1.24E+05	7.22E−06
48	32	12MPaP1	12	172	1	54.9	27.1	1.4	NA	2.04E+05	NA	1.92E+05	NA
49	32	12MPaP2	12	64	1	114.5	68.9	1.9	760	7.09E+05	1.00E+06	3.47E+05	1.88E−02
50	32	12MPaP2	12	110	2	108.9	111.9	2.9	820	1.47E+06	1.50E+06	3.69E+05	4.08E−02
51	32	12MPaP4	12	181	1	37.5	30.2	1.6	820	2.32E+05	2.76E+05	1.80E+05	1.98E−03
52	32	12MPaP4	12	224	2	82.5	93.2	2.5	1180	1.15E+06	8.60E+05	3.56E+05	3.33E−02

the contour colors cycle from light pink to dark purple every 0.1 s. Closely spaced contours with color banding indicates slow slip 1–10 μm/s. The separation of contours indicates faster slip.

Across all Poisson loading sequences, contained and partially contained events nucleated at $x \cong 2$ m, where the peak τ/σ ratio occurred (see Figure 3d and Ke et al., 2018). This relatively slow nucleation can be

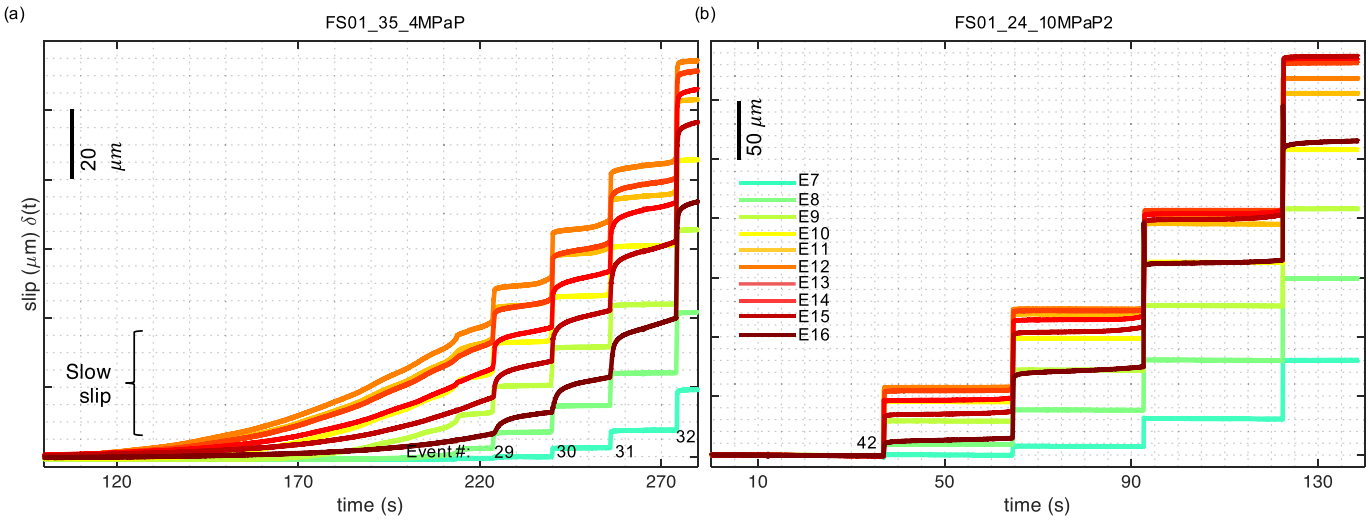

Figure 7. Slip time history of slow and fast earthquakes recorded at many locations along the 3.1 m simulated fault. (a) Before events 29–32, slip slow <0.4 μm/s occurred for about 100 s, as indicated. (b) No preceding slow slip is observed before faster event 42. E7–E16 denotes the eddy current slip sensor channels. The curves are color coded by location as shown in Figure 1b.

identified in Figure 8 by the dense set of contours that indicates slow slip in the nucleation region near $x = 2$ m. For event #29, the slip rate never exceeded 0.5 mm/s; rupture propagation velocity is poorly defined since the entire fault patch slipped nearly simultaneously. For faster events, the nucleation region was more localized in space and more abrupt in time. Many of the events did not end abruptly. Instead, they continued to slip at slow and decreasing rates (they exhibited afterslip), especially near $x = 3$ m. Event 32 slowed down and nearly arrested after only 20 μm of slip near $x = 2$ m, but then slip accelerated again for a second slip episode near $x = 3$ m.

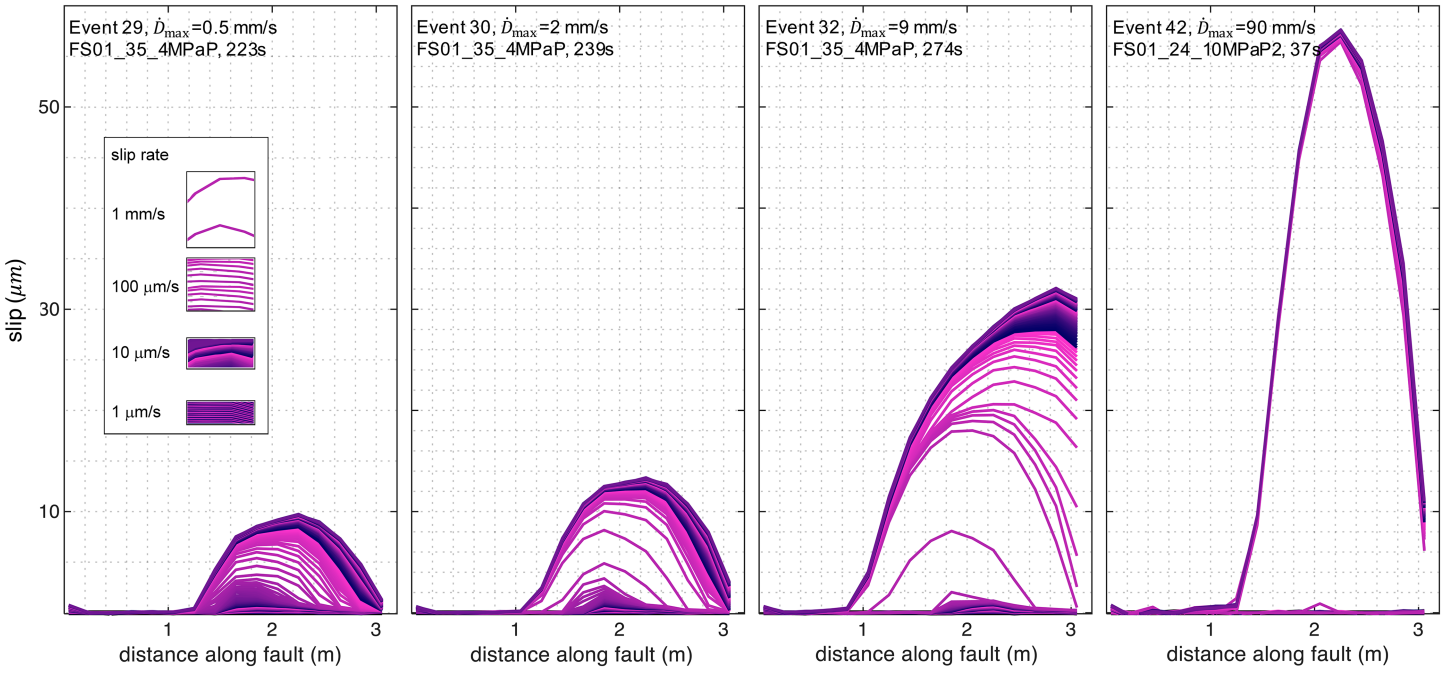

Figure 8. Spatial distribution of slip during events 29, 30, 32, and 42. Slip contours are plotted every 5 ms, while the contour color cycles from light pink to dark purple every 0.1 s. The nucleation of each event can be identified by dense contours near $x = 2$ m indicating slow slip.

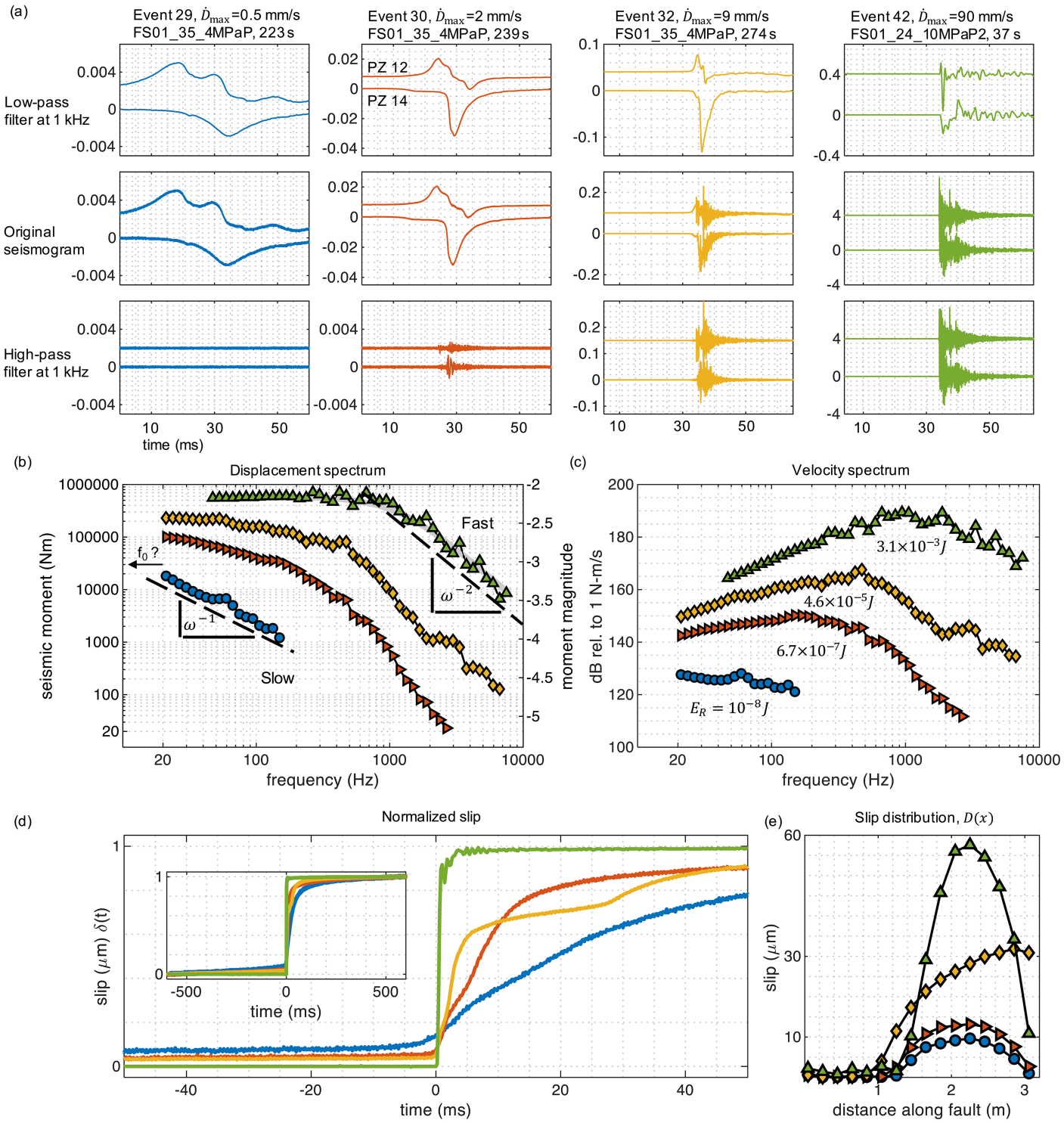

Figure 9. Seismicity and slip of four events ranging from slow (blue) to fast (green). (a) Original, high-pass filtered, and low-pass filtered waveforms of two channels of ground motions (PZ12 and PZ14). The max slip rate and experiment number are labeled. (b) Displacement source spectra for frequency bands when signal-to-noise ratio > 20 dB. (c) Velocity spectra and the radiated energy. (d) Normalized slip time history of the channel with $(\max(\dot{D}_{max}(x))$ for each event and (e) slip distribution $D(x)$. The curves are color coded through all panels.

4.3. Seismic Signatures and Radiated Energy

Figure 9 presents, for the four example events, the recorded ground motions from two sensors (PZ12 and PZ14) and source spectra. High- and low-pass filtered waveforms (cutoff at 1 kHz) are plotted in Figure 9a in addition to the original signal. The low-frequency component of the events all show a similar form, since they occur at roughly the same location on the fault (Figure 9e), but they increase in amplitude and become progressively faster with decreasing time duration (~50, 15, 5, and 2 ms, respectively). Event 29 is the slowest and does not produce any detectable high-frequency signal. For events 30 and 32, the high-frequency signal occurs after the emergent onset of the low-frequency signal. Event 42 is fastest, and high- and low-frequency components initiate essentially simultaneously.

The trends in low- and high-frequency signals are also captured by the displacement and velocity spectra (Figures 9b and 9c). The spectral shape of the fastest event (42) closely matches a Brune model with $f_0 = 1.5$ kHz, whereas the slower events (30, 32) do not match the Brune model and their corner frequencies are not well defined. The slowest event (29) exhibits an ω^{-1} spectral decay, similar to slow earthquakes in nature (Ide et al., 2007). The source duration of this event was greater than 50 ms (Figure 9d), therefore f_0 for this event was below 20 Hz and outside of the frequency band resolvable with the 2-s time window used for the Fourier transforms. The spectral differences between the slow and fast earthquakes (Events 29 and 42) are bridged by events with increasing high-frequency energy (Events 30 and 32), evident through the progression of spectral shapes. Figure 9d shows the slip time history of the four events normalized in amplitude and aligned by the time of $\dot{D}_{max}$ for each event. Events 30 and 32 have distinct subevents with slip that accelerated and decelerated several times, and this likely contributed to the poorly defined corner frequencies.

Next, we multiplied $\dot{M}(\omega)$ by $i2\pi\omega$ to obtain the velocity spectrum following Fourier transform theorems (e.g., Bracewell, 2000). From this we obtained the radiated energy $E_R = \frac{1}{4\pi^2\rho\beta^5}\int_0^{+\infty}\left|\omega\dot{M}(\omega)\right|^2 d\omega$ (e.g., Vassiliou & Kanamori, 1982), marked in Figure 9c. The changes in spectral amplitude and shape resulted in 5 orders of magnitude changes in E_R. We did not extrapolate the spectrum to a broader frequency band than shown in Figure 9, so values for E_R may be somewhat underestimated.

5. Discussion

5.1. Static Stress Drop and Max Slip Rate

Stress drop is an earthquake source parameter that has a strong influence on ground accelerations (e.g., Baltay et al., 2011; Hanks & McGuire, 1981). It is defined as the change in shear stress before and after an earthquake, but, in most cases, stress drop is not directly measurable. Instead, the spectral shape of radiated waves is measured and linked to event-averaged stress drop through an earthquake model (e.g., Boatwright, 1980; Brune, 1970; Madariaga, 1979). Stress drop is found to vary between 0.5 and 50 MPa for most standard earthquakes. Despite uncertainties in its calculation, most of this variation has been shown to represent true variation in the underlying earthquake source, at least in some cases (Baltay et al., 2011). Furthermore, no systematic dependence of stress drop on earthquake size had been shown for events ranging from **M** −7 to **M** 8 (Allmann & Shearer, 2009; Goodfellow & Young, 2014; Hanks, 1977; McLaskey et al., 2014), validating Aki's (1967) assumption of similarity between small and large earthquakes. Self-similarity may break down for large earthquakes that rupture through the entire seismogenic zone (Scholz, 1982) and for slow earthquakes (Gomberg et al., 2016).

We explore stress drop scaling relationships using $\Delta\sigma_{static}$ of ~ 40 contained and partially contained events. Figure 10 shows $\Delta\sigma_{static}$ (Equation (3)) against the max slip rate $\dot{D}_{max}$. Faster events with $\dot{D}_{max}$>10 mm/s follow a relationship $\Delta\sigma = \frac{1}{2}G\frac{\dot{D}_{max}}{\beta}$, suggested by Brune (1970) (β = 2,550 m/s is the shear wave velocity independently measured on our granite samples). Extrapolating this trend to fully seismic slip velocities (~1 m/s), we obtain a stress drop of 3 MPa, which is close to the mean stress drop found for small and large natural earthquakes (e.g., Kanamori & Anderson, 1975; Shearer et al., 2006). As a result, most of our fast events ($\dot{D}_{max}$ >10 mm/s) can be considered standard earthquakes, though, perhaps somewhat weaker than average. While higher $\overline{\sigma_n}$ tends to promote faster events in these experiments, slow events that diverge from the Brune (1970)

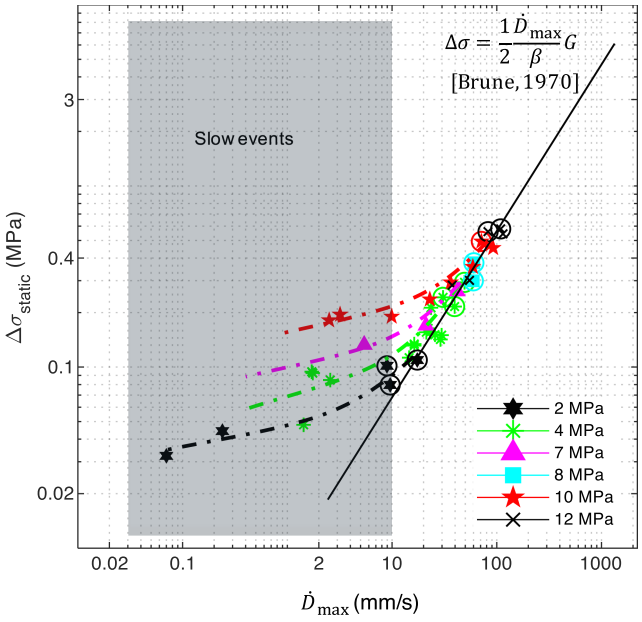

Figure 10. Static stress drop increases with the peak slip rate $\dot{D}_{max}$. Each symbol is a contained (symbols without circles) or partially contained (circled symbols) laboratory earthquake from experiments conducted at $\overline{\sigma_n}$ = 2–12 MPa. When $\dot{D}_{max}$>20 mm/s, all events follow the Brune (1970) model. Slow events have lower $\dot{D}_{max}$ for a given stress drop (blue-shaded region).

relationship can occur at nearly all $\overline{\sigma_n}$ levels (2, 4, 7, and 10 MPa), as shown by trend lines of different colors in Figure 10. At a given $\overline{\sigma_n}$, partially contained events tended to be faster and had higher stress drops than contained events, but there are no obvious indicators that their characteristics differ from the trends illustrated by the contained events.

5.2. Stress Drop and Duration

The scaling of stress drop over a wide range of earthquake sizes has been used to investigate self-similarity (Brodsky & Mori, 2007). In Figure 11, we compare $\Delta\sigma_{static}$ of contained and partially contained events generated on the Cornell 3-m apparatus to stress drops of natural earthquakes. Of these events, $\Delta\sigma$ was computed in a dynamic sense for the Cajon Pass **M** 1.4–3.4 earthquakes (Abercrombie & Rice, 2005), 50 mine earthquakes from Manitoba, Canada (Gibowicz et al., 1991) and 12 VLF earthquakes (Sugioka et al., 2012) using source parameters derived from spectral fitting or full waveform inversion. For the remaining events, $\Delta\sigma$ was computed statically using equation (3). Rupture geometry parameters (D,L) were from direct measurements (this study; Linde et al., 1996) or from kinematic finite fault inversion from geodetic data (Dragert et al., 2001, 2004; Hirose & Obara, 2005; Kostoglodov et al., 2003; Segall et al., 2006). Thomas et al. (2016) utilized both geodetic measurements and seismic information to estimate $\Delta\sigma$ of LFEs.

In both the lab and Earth, we observe a continuous spectrum of slow to fast earthquakes. Slow earthquakes observed in nature have $\Delta\sigma$ that can be orders of magnitude lower than $\Delta\sigma$ of ordinary earthquakes. Our fastest laboratory-generated earthquakes are similar to

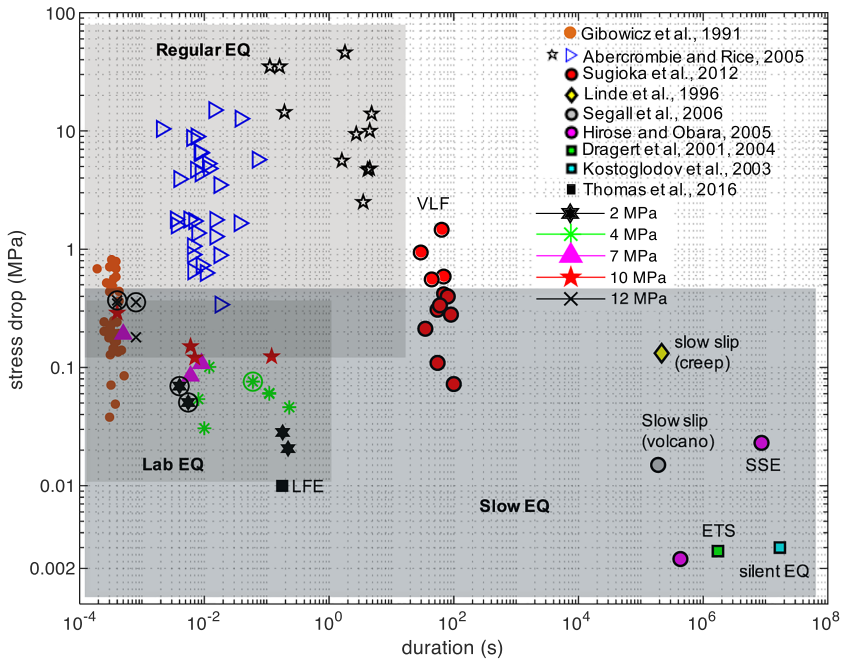

Figure 11. Static stress drop plotted against event duration. Slow earthquakes are from the deep San Andreas Fault, Hawaii, Nankai trough, Cascadia, and Mexico. The fastest contained laboratory earthquakes have similar properties to small earthquakes (Gibowicz et al., 1991), while the slower laboratory earthquakes are closer to natural low-frequency earthquakes (LFEs) and very low frequency (VLF) events.

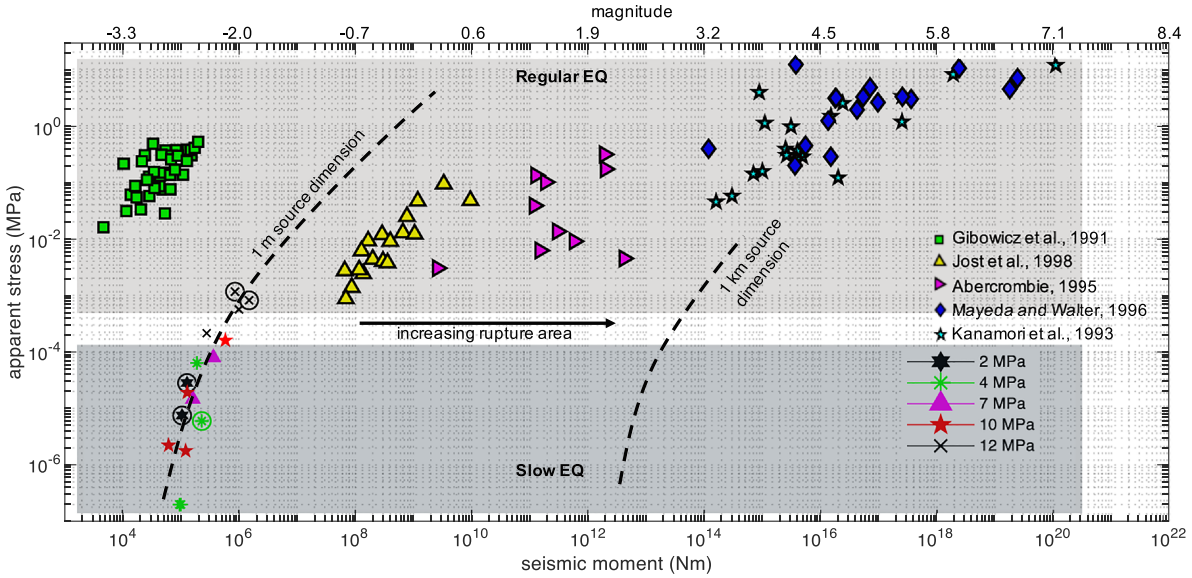

Figure 12. Apparent stress plotted against seismic moment. For laboratory-generated earthquakes, apparent stress decreases with seismic moment and max slip rate. Natural earthquakes do not have scale dependence, indicated by the red-shaded region. Each black dashed trendline shows a hypothesized nonlinear relationship between the apparent stress and seismic moment for slow-to-fast rupture of a fault patch of constant area.

microseismicity recorded in a mine (Gibowicz et al., 1991). The slower laboratory events have stress drops as low as those of VLFs and LFEs, but they are smaller and have shorter duration. Previous studies have proposed that slow and fast earthquakes may be distinct phenomena that follow different physics (Ide et al., 2007) or alternatively that they lie on a continuous spectrum of fault slip modes (Gomberg et al., 2016; Peng & Gomberg, 2010). Our integrated view of lab and natural earthquakes supports the latter view.

5.3. Radiated Energy and Apparent Stress of Slow to Fast Earthquakes

Figure 12 shows apparent stress σ_a which is a measure of radiated energy E_R relative to the seismic moment ($\sigma_a = GE_R/M_0$, (Wyss & Brune, 1968)). Ide and Beroza (2001) found σ_a to vary within 0.01–10 MPa for a compilation of earthquakes (**M** −3.5–8). Baltay et al. (2010, 2011) confirmed this result for events ranging from **M** 2–7.

The fastest contained and partially contained events generated on the Cornell 3-m apparatus have $\sigma_a = 1$ kPa, a factor of 10 lower than natural earthquakes. However, the slower laboratory-generated events have a range of σ_a that extends another 4 orders of magnitude lower, down to ~0.1 Pa for the slowest events for which E_R could still be reasonably estimated. This spread in σ_a results from 3 orders of magnitude variation in $\dot{D}_{max}$ (Table 1). As $\dot{D}_{max}$ decreases, the peak in the events' velocity source spectrum near the corner frequency is less pronounced and the apparent corner frequency decreases (see Figure 9c). Both of these effects reduce E_R and σ_a.

Another important point is that the extreme variation in radiated energy occurs with only modest variation in seismic moment. The ruptured length L has little variation. This indicates that under slightly different conditions, the same fault patch can rupture rapidly and radiate nearly as much energy as a standard earthquake, or it can rupture slowly and radiate 4 orders of magnitude less energy. The black dashed lines in Figure 12 show approximate trends for slow to fast rupture on a fault patch of constant size (~1 m for our laboratory-generated events).

Radiated energy E_R for slow earthquakes in nature has not been systematically studied due to the lack of high-sensitivity seismometers close to their sources. From the spectral record and low estimated stress drop of selected tremors (e.g., Beroza & Ide, 2011; Schwartz & Rokosky, 2007; Thomas et al., 2016), we expect E_R of slow earthquakes to be significantly lower than that of natural earthquakes.

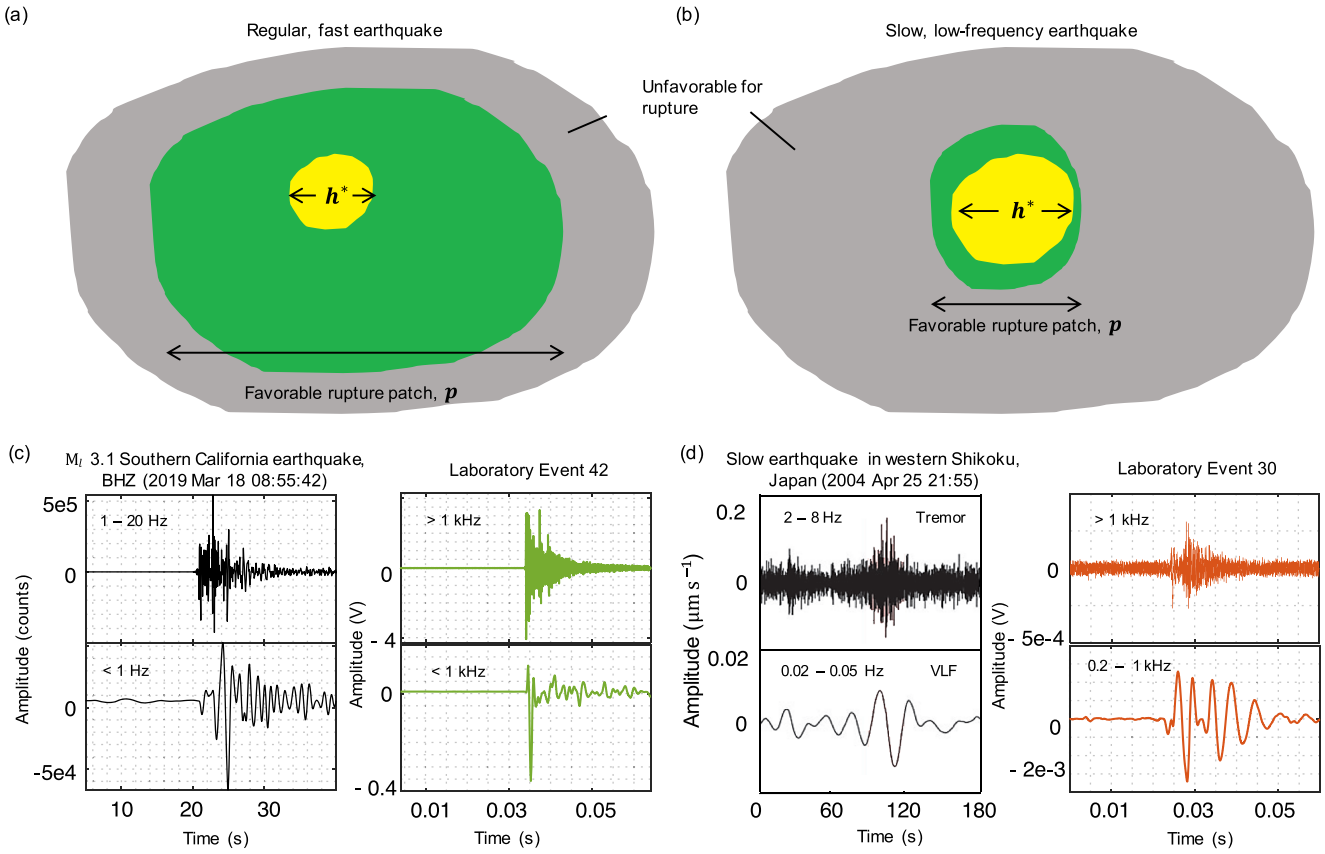

Figure 13. Schematic of mechanism to explain slow to fast earthquakes and their seismograms. (a) Large p/h^* ratio surrounded by unfavorable rupture conditions is required to produce a regular, fast earthquake. (b) Small p/h^* ratios likely characterize "tremor asperities" that produce slow low-frequency earthquakes. (c) Seismograms from fast earthquakes in the Earth and laboratory illustrate abrupt initiation and coincident high and low frequencies (filter cutoff is near f_0 for both events), (d) seismograms from slow earthquakes in the Earth and laboratory illustrate the emergent nature of wave arrivals. The M_L 3.1 Southern California earthquake is from the PFO station from the IRIS data center (http://www.iris.edu/wilber), and the Western Shikoku seismograms are from Beroza and Ide (2011).

5.4. Mechanics of Slow Earthquake Generation

The arrest of contained events on the Cornell 3-m apparatus was studied by Ke et al. (2018) who used a linear elastic fracture mechanics framework to explain rupture propagation and arrest as a balance between the energy release rate and the fracture energy. Their work indicated that rupture arrest on a fault is controlled by its potential stress drop $\Delta\tau_{pot}(x)$, defined as the initial stress on the fault $\tau_0(x)$ in excess of its residual strength $\tau_r(x)$, that is, $\Delta\tau_{pot}(x) = \tau_o(x) - \tau_r(x)$. Here, $\tau_r(x) = \mu_d\sigma_N(x)$ where μ_d is a dynamic friction level. (In Ke et al. (2018), $\tau_r(x)$ was derived from the final shear stress state $\tau_f(x)$ after a complete rupture event.) Drawing upon this framework, we denote the fault sections where $\Delta\tau_{pot} > 0$ as a "favorable rupture patch" of length p. Rupture can nucleate only within this patch and will arrest soon after propagating outside it (i.e., into sustained fault sections where $\Delta\tau_{pot}(x) < 0$).

In Figure 13 we propose a model to explain the observed spectrum of slow to fast laboratory earthquakes based on the relative lengths of the favorable rupture patch p and critical nucleation length h^*. If the ratio $\frac{p}{h^*}$ is large (Figure 13a), an earthquake rupture can accelerate to seismic levels. Under our experimental conditions, $\frac{p}{h^*} \approx 5$ (Event 42) is sufficient to produce our fastest contained lab earthquakes with parameters similar to natural ones. We expect that larger values of $\frac{p}{h^*}$ can support earthquakes with 3-MPa stress drops and 1-m/s slip speeds. If $\frac{p}{h^*} \approx 1$ (Figure 13b), then an earthquake will start to nucleate, but will fully rupture patch p and therefore begin to arrest before accelerating to fully dynamic speeds. Additionally, these slow events do not rupture like a crack or a standard, fast earthquake; the entire patch slips nearly simultaneously (Figure 8, Event 29), sometimes with multiple episodes or subevents, and the apparent

source time function is controlled by rise time. As mentioned in section 4.3, the long and poorly defined rise times correspond to events with source spectra that have f_0 that is poorly defined or lower than our resolvable frequency band.

The nucleation length scale h^* (sometimes referred to as L_c) has been found to have the form (e.g., Andrews, 1976; Dieterich, 1992; Rubin & Ampuero, 2005)

$$h^* \approx \frac{GD_c}{\sigma_n f}, \tag{5}$$

where D_c is a length scale related to fault roughness or gouge layer thickness (Marone, 1998), and f depends on details of an assumed friction relation. In laboratory experiments or numerical simulations h^* is often estimated from the size of the actively slipping region at the instant that slip rate on one part of the fault exceeds ~0.1 m/s or when the rupture velocity exceeds 10% of the shear wave velocity (e.g., Kaneko & Lapusta, 2008). It is not possible for us to quantify h^* in this way for the slower events since these exceedance criteria are never reached (the event never fully nucleates). We therefore describe h^* qualitatively in this work, and quantification of nucleation processes is reported elsewhere (G. C. McLaskey, "Earthquake initiation from laboratory observations and implications for foreshocks", submitted to Journal of Geophysical Research, 2019).

Our experiments at higher normal stress tended to produce faster events, consistent with the idea that larger σ_n promotes smaller h^* and larger p/h^*. We also observed that experiments conducted immediately after the granite blocks were reset produced more fault creep and slow events, such as Events 29–32 shown in Figures 7–9. This suggests that the reset disturbed the shear fabric of the gouge layer and temporarily increased D_c, consistent with the work of Scuderi et al. (2017) who documented systematic reduction in D_c with continued shearing of gouge layers.

In our laboratory sequences at a constant normal stress level, $\frac{p}{h^*}$ increases with successive events. This is partly due to an increase in p as the stress state is progressively smoothed by successive events, but it is also due to reduction in h^*. For example, considering Events 29–32 shown in Figure 8, p increases from ~1.8 to ~2.2 m. (We estimate p from the extent of the ruptured region.) The nucleation process also becomes more localized in both space and time with successive events (reduction in h^*), and this is partly responsible for the increasing speed of the events later in the sequence.

From equation (4), we would expect h^* to remain relatively constant in a given sequence as long as the normal stress, rigidity of the fault rocks, and friction properties remain constant, but recent experiments have shown that h^* can vary based on loading rate, healing time, and other factors (Guérin-Marthe et al., 2019; McLaskey & Yamashita, 2017). In particular, h^* has been shown to shrink in response to "kicks" such as after sudden increases in loading rate or upon resumption of loading after holding periods where the fault is held in essentially stationary contact.

The "kick"-induced variation in h^* noted above has a profound effect on radiated seismic waves, at least when $\frac{p}{h^*} \leq 1$. An example of the reduction in h^* is illustrated in Event 42 in Figure 8. This event was the first in a sequence that followed a hold of ~300 s, and its nucleation is significantly smaller and more abrupt than other events. Comparing event 42 ($\frac{p}{h^*} \approx \frac{2}{0.4} = 5$) to event 32 ($\frac{p}{h^*} \approx 1$), the factor of 5 increase in $\frac{p}{h^*}$ was accompanied by a factor of 5 increase in stress drop and a factor of 100 increase in radiated energy (Figure 9 and Table 1).

5.5. Implications for LFEs

Our slowest contained laboratory events, with $\frac{p}{h^*} < 1$, have stress drops and source durations similar to estimates from LFEs (Figure 10). In the lab, a favorable rupture patch p is set up by the heterogeneous stress conditions that result from a specific loading sequence (section 2.5). In nature, heterogeneous stress conditions would likely be erased with successive events unless there was an underlying structural feature on the fault. This "tremor asperity" could be a high normal stress "bump" or variation in fault rheology such as a velocity weakening fault patch surrounded by velocity strengthening regions. Such features would be needed to sustain the persistent locations of LFE families (e.g., Ghosh et al., 2012; Hawthorne et al., 2019; Shelly & Hardebeck, 2010; Sweet et al., 2014).

If "kick"-induced variations in stress drops and radiated energy described in section 5.4 also occur on natural faults, especially at their deeper transition between unstable and stable behavior, then the dramatic seismicity changes we observe could begin to explain some of the curious properties of LFEs and the generation of tremor in general. For example, multiple studies found that changes in the moment of LFEs were primarily due to variation in slip rather than increased rupture area (Bostock et al., 2015; Chestler & Creager, 2017). Different from typical earthquake scaling behavior, this observation suggests that a fault patch of essentially constant dimension might slip more or less under different circumstances, similar to our laboratory observations. Additionally, most tremor or LFE occurrences are correlated with high inferred slip rate or bursts of slip either at the front of a large migrating SSE (e.g., Wech & Bartlow, 2014) or from so-called rapid tremor reversals (e.g., Houston et al., 2011) and other phenomena. One possible interpretation is that LFEs are produced when the fault is "kicked" from migrating SSEs or rapid tremor reversals and this temporarily decreases h^*, increases $\frac{p}{h^*}$, and produces events with radiated energy and stress drops that are high enough for detection by seismometers.

5.6. Tremor and Other Seismic Signatures of Slow Events

The observed seismic waveforms of Events 29–32 draw resemblance to those of slow earthquakes in nature. In the Earth, tremor (2–8 Hz) and VLFs (20–50 s) are sometimes visible in a single seismic record in different frequency bands. This has been observed in western Shikoku, Japan, (Figure 2d in Beroza & Ide, 2011; Figure 3 in Ide et al., 2008) and central Alaska (Tape et al., 2018). When the seismogram for Event 30 was separated into high- and low-frequency signals, we see a tremor-like signal superposed with a VLF-like low-frequency component (Figure 13d). For the fast events, the high- and low-frequency components of the waveforms appear to act in concert (Figure 13c). For the slower events, the low-frequency components dominate, and the high-frequency components are more emergent and tremor like. However, the very low frequency ground deformation that dominates the slower events we observe in the laboratory (Figure 9a) is likely near-field deformation that decays rapidly with distance from the fault. The higher-frequency tremors may be the only part detectable at the observation distances expected for natural tectonic tremor.

6. Conclusion

By setting up a heterogeneous stress distribution on a large rock sample, we generated contained slip events that nucleate, propagate, and arrest before reaching the ends of the 3-m rock. In many ways, these events are closer to natural earthquakes than standard "stick-slip" events that rupture through an entire sample. Their dynamics are controlled by the elastic properties of the rock and the friction properties of the simulated fault, rather than by the loading machine.

The spatial distribution of slip that occurs during the contained slip events was measured in order to geodetically estimate their moment and their static stress drop. These quantities were compared to moment and stress drop estimates made from the spectra of their radiated waves derived from simultaneous measurements of ground motions. For the strongest fastest contained events generated, with $\dot{D}_{max} \approx 0.1$ m/s, the seismic and geodedic estimates of the source properties compared well: these events have $\Delta\sigma = 0.4$ MPa and source spectra are consistent with standard $\mathbf{M}$ −2.5 earthquakes. Moreover, we found slip velocity and stress drop to follow the $\Delta\sigma = \mu\dot{D}_{max}/2\beta$ relationship proposed by Brune (1970). However, we also observed a range of slower events (<10 mm/s) with low $\Delta\sigma$, inconsistent with Brune scaling, and with stress drops and source durations similar to LFEs. The spectra of the radiated waves of the slow events were depleted near the corner frequency, and this reduced their radiated energy to a weak signal reminiscent of the tremor-like signals that sometimes accompany slow earthquakes in nature. Since we generate a spectrum of fast to slow events, our work supports the idea that fast and slow earthquakes are not distinct mechanical processes, but lie on a spectrum.

The contained laboratory events only occur when the stress state along the fault is heterogeneous enough to support one fault section with conditions favorable for rupture (of length p) that is surrounded by fault sections with conditions unfavorable to rupture propagation. Successive slip events act to smooth the heterogeneous stress distribution and make way for ruptures that propagate along the full length of the fault (Ke et al., 2018). The favorable rupture patch of length p must be about 5 times larger than the critical nucleation length scale h^* for the contained events to approach seismic speeds ($\dot{D}_{max} \approx 0.1$ m/s). We find that the

ratio p/h^* has a strong influence on the speed (and consequently $\Delta\sigma$ and radiated energy) of the slip events. This study, and other recent work (Guérin-Marthe et al., 2019; McLaskey & Yamashita, 2017) has shown that h^* can vary considerably as a result of loading perturbations. Consequently, a single fault patch of length p may radiate strongly or weakly as a result of loading-dependent variation in $\frac{p}{h^*}$. If applicable to natural faults, this mechanism may help explain the puzzling way tremor is radiated.

Appendix A

We calculated the source spectrum $\dot{M}^k(\omega)$ of the kth laboratory earthquake from

$$\log\left(\dot{M}^k(\omega)\right) = \frac{1}{N}\sum_{j=1}^{N}\log\left(\frac{S_j^k(\omega)}{\Psi_j(\omega)}\right), \tag{A1}$$

where $S_j^k(\omega)$ is the Fourier transform of $s_j^k(t)$, the piezoelectric sensor output from the jth of N sensors. The parameter $\Psi_j(\omega)$ is an instrument apparatus response function defined as

$$\Psi_j(\omega) = G_j(\omega)I_j(\omega), \tag{A2}$$

and $G_j(\omega)$ and $I_j(\omega)$ are the Fourier transforms of the Green's function and instrument response ($g_j(t)$ and $i_j(t)$), respectively. A single set of instrument apparatus response functions $\Psi_j(\omega)$ was used for all events in this study. The parameter $\Psi_j(\omega)$ was determined from the recordings from both ball impact sources $S_j^{\text{ext}}(\omega)$ and laboratory earthquake sources $S_j^{\text{int}}(\omega)$ as described in equation (A4).

The ball impact was chosen as an EGF source because its source time function is a force vector $f(t)$ that can be readily and absolutely determined using Hertzian contact theory $f(t) = F_{\max}\sin(\pi t/t_c)^{3/2}$. The maximum force $F_{\max}$ and the contact duration t_c can both be determined from material properties of the ball and contact surface (Goldsmith, 2001; McLaskey & Glaser, 2010). The change in momentum Δp of the ball is both the area under the curve of $f(t)$ and the low-frequency amplitude Ω_0 of the source spectrum $F(\omega)$, and Δp can be independently calculated from the mass of the ball, its drop height, and rebound height.

A laboratory earthquake was used as an EGF source for the determination of $\Psi_j(\omega)$ for frequencies below 1 kHz, where ball impact provided insufficient signal-to-noise ratio. The source time function of an earthquake can be mathematically represented by the moment rate tensor $\dot{m}(t)$. We assume synchronous sources so that all tensor components of $\dot{m}(t)$ and vector components of $f(t)$ have identical source time functions. This allows the directionality Λ of the moment tensor and the directionality Ξ of the force vector to be separated from their time histories.

The ball source $f(t)$ acts on the surface of the rock slab, and the test source $\dot{m}(t)$ acts internal to the slab. These two types of seismic sources can be related through the constant $C_{\text{F}\dot{\text{M}}}$, the force-moment-rate scale factor

$$C_{\text{F}\dot{\text{M}}} = \frac{\dot{M}(\omega)}{F(\omega)} \tag{A3}$$

that converts momentum to moment or force to moment rate. $C_{\text{F}\dot{\text{M}}}$ is equal to 2 × the speed of sound in the granite $C_{\text{F}\dot{\text{M}}} = 5.4$ km/s (McLaskey, Lockner, et al., 2015). Equation (A3) is only valid for frequencies below the corner frequencies of both the internal source and the external source.

We characterize both ball and earthquake sources in the frequency domain (Equation (A1)), and we focus only on their amplitude spectra and ignore phase. Spectral estimates are averages of log spectra derived from signals recorded from $N = 11$ stations (11 PZ sensors) on both the top and bottom surfaces of the rock sample. We computed Fourier transforms from 2 s long time windows that included P waves, S waves, and myriad reflections and reverberations from the loading machine. This, and the averaging over multiple sensors, allows us to ignore the directionality effects of the sources such that $\Xi \cong \Lambda \cong 1$, and permits the use of equation (A3).

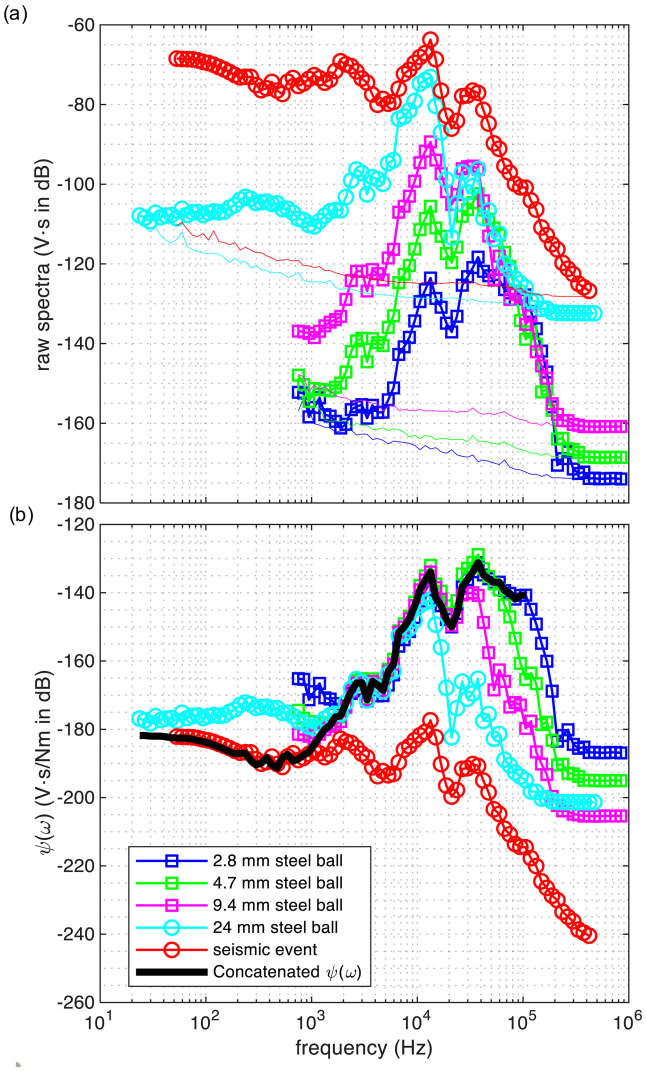

Figure A1. Deriving the instrument apparatus response $\Psi_j(\omega)$. (a) Raw spectra of the EGF events (symbols) are compared to noise spectra (no symbols). Each curve shows the average over 11 sensors. (b) Each spectrum from (a) is scaled according to equations (A4) and (A5) and provides an estimate for $\Psi_j(\omega)$ (thick black line) in frequency bands less than f_0 and where signal-to-noise ratio is greater than 20 dB.

Fourier transforming equation (2), substituting equations (A2) and (A3), and rearranging, we find

$$\Psi_j(\omega) = \frac{S_j^{\text{ext}}(\omega)}{F(\omega)C_{\text{F}\dot{\text{M}}}}, 1\text{ kHz}<\omega<10\text{ kHz} \quad \text{(A4)}$$

$$\Psi_j(\omega) = \frac{S_j^{\text{int}}(\omega)}{\dot{M}(\omega)}, 20\text{ Hz}<\omega<1\text{ kHz}. \quad \text{(A5)}$$

The determination of the instrument apparatus response $\Psi_j(\omega)$ is illustrated in Figure A1. Figure A1a shows $\frac{1}{N}\sum_{j=1}^{N}\log\left(S_j^{\text{int}}(\omega)\right)$ for one contained laboratory earthquake and $\frac{1}{N}\sum_{j=1}^{N}\log\left(S_j^{\text{ext}}(\omega)\right)$ for four collocated ball drops of various sizes. All balls were dropped onto the top surface of the granite sample with $\overline{\sigma_n}$ = 4 MPa applied to simulate actual experiment conditions. Larger balls introduce more low-frequency energy into the rock. Small balls have lower amplitude at low frequencies but extend to higher frequency due to their larger f_0. Noise spectra were also computed from a noise window of the same length, taken just before the first wave arrival. For each ball drop, we only trust its spectra when the signal-to-noise ratio is greater than 20 dB and when $\omega < f_0$. The sensors are less sensitive at lower frequencies, so for the largest ball (24 mm in diameter) $\Psi_j(\omega)$ is only valid down to 1 kHz. To extend our estimate of $\Psi_j(\omega)$ to lower frequencies (1 kHz to 20 Hz), we use a contained (Type 1) event with $f_0 \cong 1$ kHz.

Figure A1b shows the same curves as in Figure A1a except the spectrum from each ball drop is scaled by $\Delta pC_{F\dot{M}}$ (equation (A4)). (Note that $F(\omega)C_{\text{F}\dot{\text{M}}} = \Delta pC_{\text{F}\dot{\text{M}}}$ for $\omega < f_0$). The spectrum of the seismic event (red), was scaled to match the amplitude of the 24-mm steel ball at 1 kHz, since $\dot{M}(\omega)$ for that event was unknown. Once the spectra have been scaled in this way, they collapse into a common line for frequencies that are both less than f_0 and where signal-to-noise ratio is adequate. This common line $= \frac{1}{N}\sum_{j=1}^{N}\Psi_j(\omega)$ and is the heavy black line shown in Figure A1b. Once $\Psi_j(\omega)$ was determined in this way, $\dot{M}(\omega)$ for any event was found from equation (A1).

One may argue that the ball impacts and the various laboratory earthquakes are not collocated enough for the EGF method to properly remove wave propagation (path) effects. The granite is nearly isotropic and homogeneous, and since there is minimal damage in the 3-m blocks, we would not expect to find any locations with highly variable Q or wave velocity. Previous work has indicated that Rayleigh waves excited by the ball impact can bias the EGF results if not properly accounted for (McLaskey, Lockner, et al., 2015). However, this and other path effects primarily affect frequencies higher than 20 kHz. Source spectra in this study are only estimated below 10 kHz, which corresponds to wavelengths greater than 0.3 m. Consequently, all sources are spatially separated by at most a few wavelengths, and other complications such as variable fault offset produce negligible path effects. In this laboratory experiment, we believe $\Psi_j(\omega)$ is primarily affected by instrument response. Below 1 kHz, reverberations of the loading apparatus may also affect $\Psi_j(\omega)$. (Note the similarity between our results and those shown in Figure 8b of McLaskey, Lockner, et al. (2015) which utilized the same sensors but a different loading apparatus).

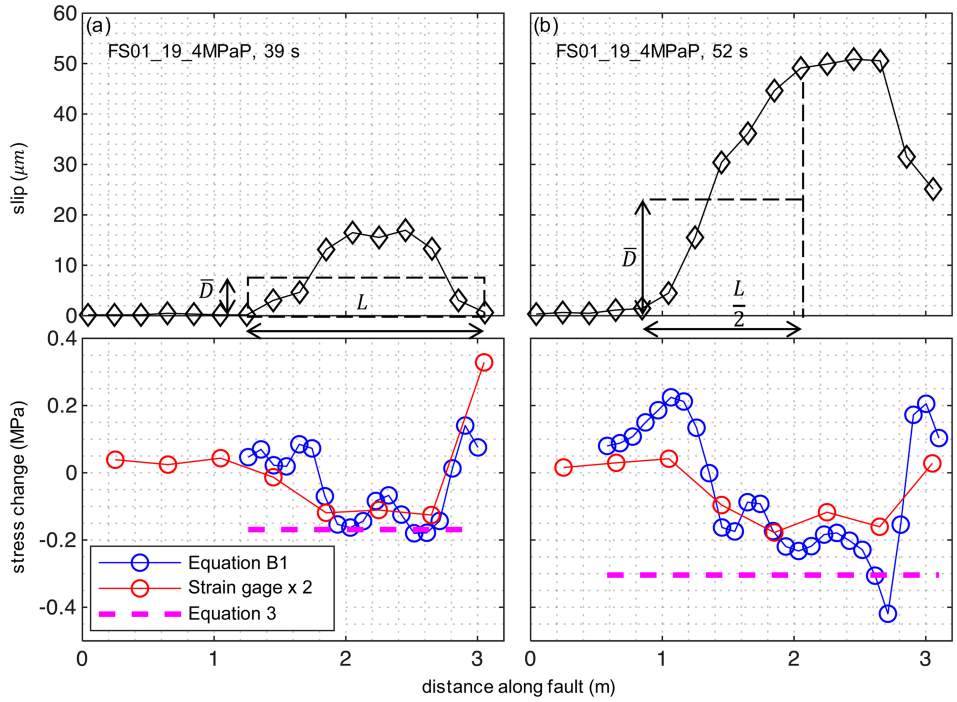

Figure B1. Measured slip profile $D(x)$ and associated stress changes for a representative (a) contained event and (b) partially contained event. The average slip $\overline{D}$ and characteristic rupture length L are labeled. Lower panels compare stress drop measured from equation (3) (magenta), strain gages (red), and calculated from slip measurements using a dislocation model from equation (B1) (blue). The amplitude of the strain gage measurements shown have been increased by a factor of 2.

Appendix B

To verify our stress drop calculations, we measured $\Delta\sigma_{static}$ using two additional methods. Bilby and Eshelby (1968) presented a dislocation model where the stress along the fault plane is expressed in terms of slip,

$$\Delta\sigma(x,t) = \frac{\mu}{2\pi(1-\nu)}\int_0^L \frac{\partial D(\xi,t)}{(x-\xi)\partial\xi}\mathrm{d}\xi. \quad \text{(B1)}$$

From this equation, we estimated stress changes from the measured slip distribution, and this is shown in Figure B1 (blue circles) and compared to $\Delta\sigma_{static}$ from equation (3) (horizontal magenta dashed line). There is good agreement between these results. We also used the strain gages at eight locations along the fault (S1–S8 in Figure 1a) to estimate stress. However, measurements from the strain gages were increased by a factor of 2 to better match the other estimates, and that is what is shown in Figure B1. We do not know the exact cause of the discrepancy. It may be related to a free surface effect or the 1.5-mm chamfer at the top corners of the block. The factor of 2 uncertainty in $\Delta\sigma_{static}$ is small compared to the measured variation in $\Delta\sigma_{static}$ (many orders of magnitude), and has little influence on the main conclusions of this work.

The two events shown in Figure B1 are representative of the population of contained and partially contained events studied. In general, stress changes within the ruptured region estimated from strain gage measurements were -0.1 ± 0.05 MPa and quite variable, and stress increased near the edges of the ruptured region. When averaged over the ruptured region, stress changes estimated from equation (B1) were consistent with equation (3), with less than a factor of 2 discrepancy.

Acknowledgments
The authors gratefully acknowledge that this work was funded by National Science Foundation Grant EAR-1645163. Data used in this paper were acquired during laboratory experiments conducted at Cornell University. Data reported here are publicly available at https://eCommons.cornell.edu using https://doi.org/10.7298/nbwb-1048. We thank C.-Y. Ke for assistance with the experiments and all strain gage data, T. Bond and J. Strait for technical assistance, and two anonymous reviewers whose comments helped improve the manuscript. The authors declare that they have no conflict of interest.

References

Abercrombie, R. E., & Rice, J. R. (2005). Can observations of earthquake scaling constrain slip weakening? *Geophysical Journal International*, *162*(2), 406–424. https://doi.org/10.1111/j.1365-246X.2005.02579.x

Aki, K. (1966). Estimation of earthquake moment, released energy, and stress-strain drop from G-wave spectrum. *Bulletin of the Earthquake Research Institute, Tokyo University*, *44*, 73–88.

Aki, K. (1967). Scaling law of seismic spectrum. *Journal of Geophysical Research*, *72*(4), 1217–1231. https://doi.org/10.1029/JZ072i004p01217

Aki, K., & Richards, P. G. (1980). *Quantitative seismology: Theory and methods* (pp. 27–59). San Francisco: Freeman.

Allmann, B. P., & Shearer, P. M. (2009). Global variations of stress drop for moderate to large earthquakes. *Journal of Geophysical Research*, *114*, B01310. https://doi.org/10.1029/2008JB005821

Andrews, D. J. (1976). Rupture velocity of plane strain shear cracks. *Journal of Geophysical Research*, *81*(32), 5679–5687. https://doi.org/10.1029/JB081i032p05679

Baltay, A., Ide, S., Prieto, G., & Beroza, G. (2011). Variability in earthquake stress drop and apparent stress. *Geophysical Research Letters*, *38*, L06303. https://doi.org/10.1029/2011GL046698

Baltay, A., Prieto, G., & Beroza, G. C. (2010). Radiated seismic energy from coda measurements and no scaling in apparent stress with seismic moment. *Journal of Geophysical Research*, *115*, B08341. https://doi.org/10.1029/2009JB006736

Ben-David, O., Rubinstein, S. M., & Fineberg, J. (2010). Slip-stick and the evolution of frictional strength. *Nature*, *463*(7277), 76–79. https://doi.org/10.1038/nature08676

Beroza, G. C., & Ide, S. (2011). Slow earthquakes and nonvolcanic tremor. *Annual Review of Earth and Planetary Sciences*, *39*(1), 271–296. https://doi.org/10.1146/annurev-earth-040809-152531

Bilby, B. A., & Eshelby, J. D. (1968). Dislocations and the theory of fracture. In H. Liebowitz (Ed.), *Fracture—An advanced treatise* (Vol. 1, Chapter 2, p. 99-182). Cambridge: Academic Press.

Boatwright, J. (1980). A spectral theory for circular seismic sources; simple estimates of source dimension, dynamic stress drop, and radiated seismic energy. *Bulletin of the Seismological Society of America*, *70*(1), 1–27.

Bostock, M. G., Thomas, A. M., Savard, G., Chuang, L., & Rubin, A. M. (2015). Magnitudes and moment-duration scaling of low-frequency earthquakes beneath southern Vancouver Island. *Journal of Geophysical Research: Solid Earth*, *120*, 6329–6350. https://doi.org/10.1002/2015JB012195

Brace, W. F., & Byerlee, J. D. (1966). Stick-slip as a mechanism for earthquakes. *Science*, *153*(3739), 990–992. https://doi.org/10.1126/science.153.3739.990

Bracewell, R. (2000). *The Fourier transforms and its applications*. Boston: McGraw-Hill.

Brodsky, E. E., & Mori, J. (2007). Creep events slip less than ordinary earthquakes. *Geophysical Research Letters*, *34*, L16309. https://doi.org/10.1029/2007GL030917

Brune, J. N. (1970). Tectonic stress and the spectra of seismic shear waves from earthquakes. *Journal of Geophysical Research*, *75*(26), 4997–5009. https://doi.org/10.1029/JB075i026p04997

Chestler, S. R., & Creager, K. C. (2017). Evidence for a scale-limited low-frequency earthquake source process. *Journal of Geophysical Research: Solid Earth*, *122*, 3099–3114. https://doi.org/10.1002/2016JB013717

Dieterich, J. H. (1981). Potential for geophysical experiments in large scale tests. *Geophysical Research Letters*, *8*(7), 653–656. https://doi.org/10.1029/GL008i007p00653

Dieterich, J. H. (1992). Earthquake nucleation on faults with rate-and state-dependent strength. *Tectonophysics*, *211*(1-4), 115–134. https://doi.org/10.1016/0040-1951(92)90055-B

Dieterich, J. H., & Kilgore, B. D. (1994). Direct observation of frictional contacts: New insights for state-dependent properties. *Pure and Applied Geophysics*, *143*(1-3), 283–302. https://doi.org/10.1007/BF00874332

Dragert, H., Wang, K., & James, T. S. (2001). A silent slip event on the deeper Cascadia subduction interface. *Science*, *292*(5521), 1525–1528. https://doi.org/10.1126/science.1060152

Dragert, H., Wang, K., & Rogers, G. (2004). Geodetic and seismic signatures of episodic tremor and slip in the northern Cascadia subduction zone. *Earth, Planets and Space*, *56*(12), 1143–1150. https://doi.org/10.1186/BF03353333

Ghosh, A., Huesca-Pérez, E., Brodsky, E., & Ito, Y. (2015). Very low frequency earthquakes in Cascadia migrate with tremor. *Geophysical Research Letters*, *42*, 3228–3232. https://doi.org/10.1002/2015GL063286

Ghosh, A., Vidale, J. E., & Creager, K. C. (2012). Tremor asperities in the transition zone control evolution of slow earthquakes. *Journal of Geophysical Research*, *117*, B10301. https://doi.org/10.1029/2012JB009249

Gibowicz, S. J., Young, R. P., Talebi, S., & Rawlence, D. J. (1991). Source parameters of seismic events at the Underground Research Laboratory in Manitoba, Canada: Scaling relations for events with moment magnitude smaller than −2. *Bulletin of the Seismological Society of America*, *81*(4), 1157–1182.

Goldsmith, W. (2001). *Impact*. New York: Dover Publications.

Gomberg, J., Wech, A., Creager, K., Obara, K., & Agnew, D. (2016). Reconsidering earthquake scaling. *Geophysical Research Letters*, *43*, 6243–6251. https://doi.org/10.1002/2016GL069967

Goodfellow, S. D., & Young, R. P. (2014). A laboratory acoustic emission experiment under in situ conditions. *Geophysical Research Letters*, *41*, 3422–3430. https://doi.org/10.1002/2014GL059965

Guérin-Marthe, S., Nielsen, S., Bird, R., Giani, S., & Di Toro, G. (2019). Earthquake nucleation size: Evidence of loading rate dependence in laboratory faults. *Journal of Geophysical Research: Solid Earth*, *124*, 689–708. https://doi.org/10.1029/2018JB016803

Hanks, T. C. (1977). Earthquake stress drops, ambient tectonic stresses and stresses that drive plate motions. In *Stress in the Earth* (pp. 441–458). Basel: Birkhäuser. https://doi.org/10.1007/978-3-0348-5745-1_28

Hanks, T. C., & McGuire, R. K. (1981). The character of high-frequency strong ground motion. *Bulletin of the Seismological Society of America*, *71*(6), 2071–2095.

Hawthorne, J., Thomas, A., & Ampuero, J.-P. (2019). The rupture extent of low frequency earthquakes near Parkfield, CA. *Geophysical Journal International*, *216*(1), 621–639. https://doi.org/10.1093/gji/ggy429

Hirose, H., Hirahara, K., Kimata, F., Fujii, N., & Miyazaki, S. I. (1999). A slow thrust slip event following the two 1996 Hyuganada earthquakes beneath the Bungo Channel, southwest Japan. *Geophysical Research Letters*, *26*(21), 3237–3240. https://doi.org/10.1029/1999GL010999

Hirose, H., & Obara, K. (2005). Repeating short-and long-term slow slip events with deep tremor activity around the Bungo channel region, southwest Japan. *Earth, Planets and Space*, *57*(10), 961–972. https://doi.org/10.1186/BF03351875

Houston, H., Delbridge, B. G., Wech, A. G., & Creager, K. C. (2011). Rapid tremor reversals in Cascadia generated by a weakened plate interface. *Nature Geoscience*, *4*(6), 404–409. https://doi.org/10.1038/ngeo1157

Ide, S., & Beroza, G. C. (2001). Does apparent stress vary with earthquake size? *Geophysical Research Letters*, *28*(17), 3349–3352. https://doi.org/10.1029/2001GL013106

Ide, S., Beroza, G. C., Shelly, D. R., & Uchide, T. (2007). A scaling law for slow earthquakes. *Nature*, *447*(7140), 76–79. https://doi.org/10.1038/nature05780

Ide, S., Imanishi, K., Yoshida, Y., Beroza, G. C., & Shelly, D. R. (2008). Bridging the gap between seismically and geodetically detected slow earthquakes. *Geophysical Research Letters*, *35*, L10305. https://doi.org/10.1029/2008GL034014

Johnson, T., Wu, F. T., & Scholz, C. H. (1973). Source parameters for stick-slip and for earthquakes. *Science*, *179*(4070), 278–280. https://doi.org/10.1126/science.179.4070.278

Johnson, T. L., & Scholz, C. H. (1976). Dynamic properties of stick-slip friction of rock. *Journal of Geophysical Research*, *81*(5), 881–888. https://doi.org/10.1029/JB081i005p00881

Kanamori, H., & Anderson, D. L. (1975). Theoretical basis of some empirical relations in seismology. *Bulletin of the Seismological Society of America*, *65*(5), 1073–1095.

Kaneko, Y., & Lapusta, N. (2008). Variability of earthquake nucleation in continuum models of rate-and-state faults and implications for aftershock rates. *Journal of Geophysical Research*, *113*, B12312. https://doi.org/10.1029/2007JB005154

Kaproth, B. M., & Marone, C. (2013). Slow earthquakes, preseismic velocity changes, and the origin of slow frictional stick-slip. *Science*, *341*(6151), 1229–1232. https://doi.org/10.1126/science.1239577

Kato, N., Yamamoto, K., Yamamoto, H., & Hirasawa, T. (1992). Strain-rate effect on frictional strength and the slip nucleation process. *Tectonophysics*, *211*(1-4), 269–282. https://doi.org/10.1016/0040-1951(92)90064-D

Ke, C. Y., McLaskey, G. C., & Kammer, D. S. (2018). Rupture termination in laboratory-generated earthquakes. *Geophysical Research Letters*, *45*, 12–784. https://doi.org/10.1029/2018GL080492

Knopoff, L. (1958). Energy release in earthquakes. *Geophysical Journal International*, *1*(1), 44–52. https://doi.org/10.1111/j.1365-246X.1958.tb00033.x

Kostoglodov, V., Singh, S. K., Santiago, J. A., Franco, S. I., Larson, K. M., Lowry, A. R., & Bilham, R. (2003). A large silent earthquake in the Guerrero seismic gap, Mexico. *Geophysical Research Letters*, *30*(15), 1807. https://doi.org/10.1029/2003GL017219

Leeman, J. R., Saffer, D. M., Scuderi, M. M., & Marone, C. (2016). Laboratory observations of slow earthquakes and the spectrum of tectonic fault slip modes. *Nature Communications*, *7*(1), 1–6. https://doi.org/10.1038/ncomms11104

Linde, A. T., Gladwin, M. T., Johnston, M. J., Gwyther, R. L., & Bilham, R. G. (1996). A slow earthquake sequence on the San Andreas Fault. *Nature*, *383*(6595), 65–68. https://doi.org/10.1038/383065a0

Liu, Y., & Rice, J. R. (2005). Aseismic slip transients emerge spontaneously in three-dimensional rate and state modeling of subduction earthquake sequences. *Journal of Geophysical Research*, *110*, B08307. https://doi.org/10.1029/2004JB003424

Lockner, D. A., Okubo, P. G., & Dieterich, J. H. (1982). Containment of stick-slip failures on a simulated fault by pore fluid injection. *Geophysical Research Letters*, *9*(8), 801–804. https://doi.org/10.1029/GL009i008p00801

Madariaga, R. (1979). On the relation between seismic moment and stress drop in the presence of stress and strength heterogeneity. *Journal of Geophysical Research*, *84*(B5), 2243–2250. https://doi.org/10.1029/JB084iB05p02243

Marone, C. (1998). Laboratory-derived friction laws and their application to seismic faulting. *Annual Review of Earth and Planetary Sciences*, *26*(1), 643–696. https://doi.org/10.1146/annurev.earth.26.1.643

McLaskey, G., & Glaser, S. (2010). Hertzian impact: experimental study of the force pulse and resulting stress waves. *The Journal of the Acoustical Society of America*, *128*(3), 1087–1096. https://doi.org/10.1121/1.3466847

McLaskey, G. C., & Kilgore, B. D. (2013). Foreshocks during the nucleation of stick-slip instability. *Journal of Geophysical Research: Solid Earth*, *118*, 2982–2997. https://doi.org/10.1002/jgrb.50232

McLaskey, G. C., Kilgore, B. D., & Beeler, N. M. (2015). Slip-pulse rupture behavior on a 2 m granite fault. *Geophysical Research Letters*, *42*, 7039–7045. https://doi.org/10.1002/2015GL065207

McLaskey, G. C., Kilgore, B. D., Lockner, D. A., & Beeler, N. M. (2014). Laboratory generated M-6 earthquakes. *Pure and Applied Geophysics*, *171*(10), 2601–2615. https://doi.org/10.1007/s00024-013-0772-9

McLaskey, G. C., Lockner, D. A., Kilgore, B. D., & Beeler, N. M. (2015). A robust calibration technique for acoustic emission systems based on momentum transfer from a ball drop. *Bulletin of the Seismological Society of America*, *105*(1), 257–271. https://doi.org/10.1785/0120140170

McLaskey, G. C., & Yamashita, F. (2017). Slow and fast ruptures on a laboratory fault controlled by loading characteristics. *Journal of Geophysical Research: Solid Earth*, *122*, 3719–3738. https://doi.org/10.1002/2016JB013681

Mogi, K. (1968). Sequential occurrences of recent great earthquakes. *Journal of Physics of the Earth*, *16*(1), 30–36. https://doi.org/10.4294/jpe1952.16.30

Nielsen, S., Taddeucci, J., & Vinciguerra, S. (2010). Experimental observation of stick-slip instability fronts. *Geophysical Journal International*, *180*(2), 697–702. https://doi.org/10.1111/j.1365-246X.2009.0444.x

Obara, K. (2002). Nonvolcanic deep tremor associated with subduction in southwest Japan. *Science*, *296*(5573), 1679–1681. https://doi.org/10.1126/science.1070378

Obara, K., & Kato, A. (2016). Connecting slow earthquakes to huge earthquakes. *Science*, *353*(6296), 253–257. https://doi.org/10.1126/science.aaf1512

Ohnaka, M., & Kuwahara, Y. (1990). Characteristic features of local breakdown near a crack-tip in the transition zone from nucleation to unstable rupture during stick-slip shear failure. *Tectonophysics*, *175*(1-3), 197–220. https://doi.org/10.1016/0040-1951(90)90138-X

Okubo, P. G., & Dieterich, J. H. (1984). Effects of physical fault properties on frictional instabilities produced on simulated faults. *Journal of Geophysical Research*, *89*(B7), 5817–5827. https://doi.org/10.1029/JB089iB07p05817

Peng, Z., & Gomberg, J. (2010). An integrated perspective of the continuum between earthquakes and slow-slip phenomena. *Nature Geoscience*, *3*(9), 599–607. https://doi.org/10.1038/ngeo940

Rogers, G., & Dragert, H. (2003). Episodic tremor and slip on the Cascadia subduction zone: The chatter of silent slip. *Science*, *300*(5627), 1942–1943. https://doi.org/10.1126/science.1084783

Rosakis, A. J., Kanamori, H., & Xia, K. (2006). Laboratory earthquakes. In *Advances in fracture research* (pp. 211–218). Dordrecht: Springer. https://doi.org/10.1007/s10704-006-0030-6

Rubin, A. M., & Ampuero, J. P. (2005). Earthquake nucleation on (aging) rate and state faults. *Journal of Geophysical Research*, *110*, B11312. https://doi.org/10.1029/2005JB003686

Ruina, A. (1983). Slip instability and state variable friction laws. *Journal of Geophysical Research*, *88*(B12), 10,359–10,370. https://doi.org/10.1029/JB088iB12p10359

Scholz, C. H. (1982). Scaling laws for large earthquakes: Consequences for physical models. *Bulletin of the Seismological Society of America*, *72*(1), 1–14.

Scholz, C. H. (1988). The brittle-plastic transition and the depth of seismic faulting. *Geologische Rundschau*, *77*(1), 319–328. https://doi.org/10.1007/BF01848693

Schwartz, S. Y., & Rokosky, J. M. (2007). Slow slip events and seismic tremor at circum-Pacific subduction zones. *Reviews of Geophysics*, *45*, RG3004. https://doi.org/10.1029/2006RG000208

Scuderi, M. M., Collettini, C., Viti, C., Tinti, E., & Marone, C. (2017). Evolution of shear fabric in granular fault gouge from stable sliding to stick slip and implications for fault slip mode. *Geology*, *45*(8), 731–734. https://doi.org/10.1130/G39033.1

Scuderi, M. M., Marone, C., Tinti, E., Di Stefano, G., & Collettini, C. (2016). Precursory changes in seismic velocity for the spectrum of earthquake failure modes. *Nature Geoscience*, *9*(9), 695–700. https://doi.org/10.1038/ngeo2775

Segall, P., Desmarais, E. K., Shelly, D., Miklius, A., & Cervelli, P. (2006). Earthquakes triggered by silent slip events on Kīlauea volcano, Hawaii. *Nature*, *442*(7098), 71–74. https://doi.org/10.1038/nature04938

Selvadurai, P., & Glaser, S. (2017). Asperity generation and its relationship to seismicity on a planar fault: A laboratory simulation. *Geophysical Journal International*, *208*(2), 1009–1025. https://doi.org/10.1093/gji/ggw439

Shearer, P. M., Prieto, G. A., & Hauksson, E. (2006). Comprehensive analysis of earthquake source spectra in southern California. *Journal of Geophysical Research*, *111*, B06303. https://doi.org/10.1029/2005JB003979

Shelly, D. R., Beroza, G. C., & Ide, S. (2007). Non-volcanic tremor and low-frequency earthquake swarms. *Nature*, *446*(7133), 305–307. https://doi.org/10.1038/nature05666

Shelly, D. R., & Hardebeck, J. L. (2010). Precise tremor source locations and amplitude variations along the lower-crustal central San Andreas Fault. *Geophysical Research Letters*, *37*, L14301. https://doi.org/10.1029/2010GL043672

Stein, S., & Wysession, M. (2003). *An introduction to seismology, earthquakes and Earth Structure*. (p. 242). Australia: Blackwell Publishing.

Sugioka, H., Okamoto, T., Nakamura, T., Ishihara, Y., Ito, A., Obana, K., et al. (2012). Tsunamigenic potential of the shallow subduction plate boundary inferred from slow seismic slip. *Nature Geoscience*, *5*(6), 414–418. https://doi.org/10.1038/ngeo1466

Sweet, J. R., Creager, K. C., & Houston, H. (2014). A family of repeating low-frequency earthquakes at the downdip edge of tremor and slip. *Geochemistry, Geophysics, Geosystems*, *15*, 3713–3721. https://doi.org/10.1002/2014GC005449

Tape, C., Holtkamp, S., Silwal, V., Hawthorne, J., Kaneko, Y., Ampuero, J. P., et al. (2018). Earthquake nucleation and fault slip complexity in the lower crust of central Alaska. *Nature Geoscience*, *11*(7), 536–541. https://doi.org/10.1038/s41561-018-0144-2

Thomas, A. M., Beroza, G. C., & Shelly, D. R. (2016). Constraints on the source parameters of low-frequency earthquakes on the San Andreas Fault. *Geophysical Research Letters*, *43*, 1464–1471. https://doi.org/10.1002/2015GL067173

Togo, T., Shimamoto, T., Yamashita, F., Fukuyama, E., Mizoguchi, K., & Urata, Y. (2015). Stick–slip behavior of Indian gabbro as studied using a NIED large-scale biaxial friction apparatus. *Earthquake Science*, *28*(2), 97–118. https://doi.org/10.1007/s11589-015-0113-4

Vassiliou, M. S., & Kanamori, H. (1982). The energy release in earthquakes. *Bulletin of the Seismological Society of America*, *72*(2), 371–387.

Wech, A. G., & Bartlow, N. M. (2014). Slip rate and tremor genesis in Cascadia. *Geophysical Research Letters*, *41*, 392–398. https://doi.org/10.1002/2013GL058607

Wu, B. S., & McLaskey, G. C. (2018). Broadband calibration of acoustic emission and ultrasonic sensors from generalized ray theory and finite element models. *Journal of Nondestructive Evaluation*, *37*(1), 8. https://doi.org/10.1007/s10921-018-0462-8

Wyss, M., & Brune, J. N. (1968). Seismic moment, stress, and source dimensions for earthquakes in the California-Nevada region. *Journal of Geophysical Research*, *73*(14), 4681–4694. https://doi.org/10.1029/JB073i014p04681

Yamashita, F., Fukuyama, E., Xu, S., Mizoguchi, K., Kawakata, H., & Takizawa, S. (2018). Rupture preparation process controlled by surface roughness on meter-scale laboratory fault. *Tectonophysics*, *733*, 193–208. https://doi.org/10.1016/j.tecto.2018.01.034